

Outflows from Super Star Clusters in the Central Starburst of NGC 253

Rebecca C. Levy¹, Alberto D. Bolatto¹, Adam K. Leroy², Kimberly L. Emig^{3,4,13}, Mark Gorski⁵, Nico Krieger⁶, Laura Lenkić , David S. Meier , Elisabeth A. C. Mills , Jürgen Ott , Erik Rosolowsky , Elizabeth Tarantino , Elizabeth Tarantino , Sylvain Veilleux 1, Fabian Walter 6,8, Axel Weiß 1, and Martin A. Zwaan 12, and A. Zwaan Department of Astronomy, University of Maryland, College Park, MD 20742, USA; rlevy@astro.umd.edu Department of Astronomy, The Ohio State University, Columbus, OH 43210, USA ³ Leiden Observatory, Leiden University, P.O. Box 9513, 2300-RA Leiden, The Netherlands ⁴ National Radio Astronomy Observatory, 520 Edgemont Road, Charlottesville, VA 22903-2475, USA Chalmers University of Technology, Gothenburg, Sweden ⁶ Max-Planck-Institut für Astronomie, Königstuhl 17, D-69120 Heidelberg, Germany ⁷ Department of Physics, New Mexico Institute of Mining and Technology, 801 Leroy Place, Socorro, NM, 87801, USA National Radio Astronomy Observatory, P.O. Box O, 1003 Lopezville Road, Socorro, NM 87801, USA Department of Physics and Astronomy, University of Kansas, 1251 Wescoe Hall Drive, Lawrence, KS 66045, USA Department of Physics, University of Alberta, 4-183 CCIS, Edmonton, Alberta, T6G 2E1, Canada Max-Planck-Institut für Radioastronomie, Auf dem Hügel 69, D-53121 Bonn, Germany ¹² European Southern Observatory, Karl-Schwarzschildstrasse 2, D-85748 Garching Bei Muenchen, Germany Received 2020 November 9; revised 2021 March 4; accepted 2021 March 6; published 2021 April 29

Abstract

Young massive clusters play an important role in the evolution of their host galaxies, and feedback from the highmass stars in these clusters can have profound effects on the surrounding interstellar medium. The nuclear starburst in the nearby galaxy NGC 253 at a distance of 3.5 Mpc is a key laboratory in which to study star formation in an extreme environment. Previous high-resolution (1.9 pc) dust continuum observations from the Atacama Large Millimeter/submillimeter Array (ALMA) discovered 14 compact, massive super star clusters (SSCs) still in formation. We present here ALMA data at 350 GHz with 28 mas (0.5 pc) resolution. We detect blueshifted absorption and redshifted emission (P-Cygni profiles) toward three of these SSCs in multiple lines, including CS 7–6 and H¹³CN 4–3, which represent direct evidence for previously unobserved outflows. The mass contained in these outflows is a significant fraction of the cluster gas masses, which suggests we are witnessing a short but important phase. Further evidence of this is the finding of a molecular shell around the only SSC visible at near-IR wavelengths. We model the P-Cygni line profiles to constrain the outflow geometry, finding that the outflows must be nearly spherical. Through a comparison of the outflow properties with predictions from simulations, we find that none of the available mechanisms completely explains the observations, although dust-reprocessed radiation pressure and O star stellar winds are the most likely candidates. The observed outflows will have a very substantial effect on the clusters' evolution and star formation efficiency.

Unified Astronomy Thesaurus concepts: Starburst galaxies (1570); Interstellar medium (847); Star clusters (1567); Young massive clusters (2049); Stellar feedback (1602); Galaxies (573); Interstellar molecules (849); Star formation (1569)

1. Introduction

Many stages of the stellar life cycle inject energy and momentum into the surrounding medium. For young clusters of stars, this feedback can alter the properties of the cluster itself in addition to the host galaxy. Outflows from young clusters, in particular, remove gas that may have otherwise formed more stars, affecting the star formation efficiency (SFE) of the cluster. The gas-clearing process can proceed through a number of physical mechanisms that are efficient over different density regimes and timescales, such as photoionization, radiation pressure, supernovae, and stellar winds. Outflows from forming massive clusters have been observed in the Large Magellanic Cloud (Nayak et al. 2019) and in the Antennae (Gilbert & Graham 2007; Herrera & Boulanger 2017).

At high levels of star formation, a larger fraction of stars form in clustered environments (Kruijssen 2012; Johnson et al. 2016; Ginsburg & Kruijssen 2018). The most extreme star-forming environments can lead to massive $(M_*>10^5~M_\odot)$ and compact $(r\sim 1~{\rm pc})$ so-called "super" star clusters (SSCs; e.g.,

Portegies Zwart et al. 2010). Because they are often deeply embedded, observations of young SSCs in the process of forming are rare (e.g., Keto et al. 2005; Herrera & Boulanger 2017; Oey et al. 2017; Turner et al. 2017; Leroy et al. 2018; Emig et al. 2020). Observations and simulations both indicate that SSCs should have high SFEs (e.g., Skinner & Ostriker 2015; Oey et al. 2017; Turner et al. 2017; Krumholz et al. 2019; Lancaster et al. 2021a, 2021b). Given these high SFEs, by what process(es) do these SSCs disperse their natal gas?

NGC 253 is an ideal target to study massive, clustered star formation in detail. It is one of the nearest ($d \sim 3.5$ Mpc; Rekola et al. 2005) starburst galaxies forming stars at a rate of $\sim 2 \, M_\odot \, {\rm yr}^{-1}$ in the central kiloparsec (Bendo et al. 2015; Leroy et al. 2015). The star formation is concentrated in dense clumps, knots, and clouds of gas (Turner & Ho 1985; Ulvestad & Antonucci 1997; Paglione et al. 2004; Sakamoto et al. 2006, 2011; Bendo et al. 2015; Leroy et al. 2015; Ando et al. 2017). Recent high-resolution data from the Atacama Large Millimeter/submillimeter Array (ALMA) reveal at least 14 dusty, massive proto-SSCs (Leroy et al. 2018) at the heart of these larger dense gas structures. Moreover, the clusters themselves have radio recombination line (RRL) and radio

¹³ Jansky Fellow of the National Radio Astronomy Observatory.

continuum emission (E. A. C. Mills et al. 2021, in preparation), further confirmation that these are young clusters.

However, even at the 1.9 pc (0.11") resolution of the previous study by Leroy et al. (2018), the clusters, which have radii of 0.6–1.5 pc, are only marginally resolved. Even higher resolution data are needed to spatially resolve these compact clusters to study the cluster-scale kinematics and feedback.

Here, we present direct evidence for massive outflows from three forming SSCs in the center of NGC 253 using new, very high-resolution ($0.028''\approx 0.48~\mathrm{pc}\approx 10^5~\mathrm{au}$) data from ALMA at 350 GHz. These three clusters show blueshifted absorption and redshifted emission line profiles—P-Cygni profiles—in several lines. Our analysis shows that these profiles are a direct signature of massive outflows from these SSCs. We briefly describe the observations, data processing, and imaging in Section 2. We present measured properties of the outflows from three SSCs based on the line profiles and modeling in Section 3. We discuss the relevant timescales of the outflows and clusters in terms of their evolutionary stage, mechanisms to power the outflows, and comment on the specific case of SSC 5—which is the only cluster visible in the near-infrared (NIR)—in Section 4. We summarize our findings in Section 5.

The analysis in this paper will be focused on the three clusters with clear P-Cygni profiles: SSCs 4a, 5a, and 14. We will focus on results obtained from the CS 7-6 and H¹³CN 4 -3 lines for the following reasons. First, these lines show bright emission toward many of the SSCs and are detected at a relatively high signal-to-noise ratio (S/N). Because of their high critical densities ($n_{\rm crit} \sim 3-5 \times 10^6 {\rm cm}^{-3}$ and $n_{\rm crit} \sim 0.8-2 \times 10^7 {\rm cm}^{-3}$, respectively; Shirley 2015), they probe gas that is more localized to the clusters themselves, lessening uncertainties introduced by the foreground gas correction (Section 2.4). In the case of $H^{13}CN$ 4–3, the ¹³C/¹²C isotopic ratio means this line is even less likely to be very optically thick. Although strong, the CO 3-2 line shape is complicated because it has components from clouds along the line of sight that are not associated with the clusters. Though the HCN 4-3 and HCO⁺4-3 lines are bright and also have high critical densities $(n_{\rm crit} \sim 0.9-3 \times 10^7 \, {\rm cm}^{-3})$ and $n_{\rm crit} \sim$ $2-3.6 \times 10^6$ cm⁻³, respectively; Shirley 2015), they are more abundant and more optically thick than CS 7-6 and H¹³CN 4 -3, and the absorption components in these lines suffer from saturation (i.e., absorption down to zero). This makes determining physical quantities of the outflows—which rely on the absorption depth to continuum ratio (Section 3)—difficult and uncertain. Therefore, we find that the CS 7-6 and H¹³CN 4-3 lines provide the best balance between bright lines with sufficient S/N, absorption features that do not suffer from saturation effects and that probe gas localized to the clusters to minimize uncertainties from the foreground gas correction.

2. Observations, Data Processing, and Outflow Identification

Data for this project were taken with ALMA as part of project 2017.1.00433.S (P.I. A. Bolatto). We observed the central 16.64" (280 pc) of NGC 253 at Band 7 ($\nu \sim 350$ GHz, $\lambda \sim 0.85~\mu m$) using the main 12 m array in the C43-9 configuration. This configuration resulted in baselines spanning from 113 m–13.9 km and hence a maximum recoverable scale of 0.38" (6.4 pc). The spectral setup is identical to our previous observations of this region (Leroy et al. 2018; Krieger et al. 2019, 2020), spanning frequency ranges of

342.08–345.78 GHz in the lower sideband and 353.95–357.66 GHz in the upper sideband. Observations were taken on 2017 November 9–11 with a total observing time of 5.7 hr of which 2.0 hr were on-source. The visibilities were pipeline calibrated using the Common Astronomy Software Application (CASA; McMullin et al. 2007) version 5.1.1–5 (L. Davis et al. 2021, in preparation). J0038–2459 was the phase calibrator, and J0006–0623 was the bandpass and flux calibrator.

2.1. Imaging the Continuum

In this paper, we focus on the line profiles, specifically the CS 7–6 and H¹³CN 4–3 lines toward three of the SSCs. We will present the continuum data more fully in a forthcoming paper (R. C. Levy et al. 2021, in preparation). Some of the data are presented and used here, and we provide a brief summary.

To extract the 350 GHz continuum data, we flagged channels that may contain strong lines in the band, assuming a systemic velocity of 243 km s⁻¹ (Koribalski et al. 2004). Lines included in the flagging are ¹²CO 3–2, HCN 4–3, H¹³CN 4–3, CS 7 -6, HCO⁺ 4-3, 29 SiO 8-7, and 12 CO 3-2 v = 1 (though this line is not detected), and channels within $\pm 200 \,\mathrm{km \, s^{-1}}$ of the rest frequencies of these lines were flagged. We imaged the line-flagged visibilities using the CASA version 5.4.1 tclean task with specmode = 'mfs', deconvolver='multiscale', scales=[0,4,16,64], Briggs weighting with robust = 0.5, and no uv-taper. The baseline was fit with a linear function (nterms = 2) to account for any change in slope over the wide band. The continuum was cleaned down to a threshold of $27 \mu \text{Jy beam}^{-1}$, after which the residuals resembled noise. This map has a beam size of $0.024'' \times 0.016''$ and a cell (pixel) size of 0.0046" (0.078 pc), so that we place around 4 pixels across the minor axis of the beam. Finally, the map was convolved to a circular beam size of 0.028" (0.48 pc). The rms noise of the continuum image (away from emission) is $26 \,\mu\text{Jy beam}^{-1} \ (0.3 \text{ K}).$

From this high-resolution 350 GHz continuum image (Figure 1), we identify approximately three dozen clumps of dust emission. These are co-spatial with the 14 proto-SSCs identified by Leroy et al. (2018), with many sources breaking apart into smaller clumps that likely represent individual clusters. We note that there is appreciable overlap in the spatial scales probed by these observations and those presented by Leroy et al. (2018). This means that the larger cluster sizes measured by Leroy et al. (2018) are due to the lower resolution, with the true cluster sizes better traced by these observations. We further verify this by computing the fluxes in the high-resolution continuum image in the same apertures used by Leroy et al. (2018, see their Table 1). For SSCs 4, 5, and 14 (the focus of this analysis), we recover >80% of the reported flux

We follow the SSC naming convention of Leroy et al. (2018), adding letters to denote subclusters in decreasing order of brightness. For clusters that break apart, there is always a main, brightest cluster. For example, SSC 4 from Leroy et al. (2018) breaks apart into six dust clumps, where the peak intensity of SSC 4a is $>4\times$ that of any of the smaller clumps. For this paper, we will focus only on the primary clusters since those are the most massive, and smaller dust clumps may not be true clusters. We also remove SSC 6 from this analysis, as it is extended and more tenuous in the high-resolution continuum map and so may not be an SSC. Leroy et al. (2018) also noted that this clump is weak and may instead be a

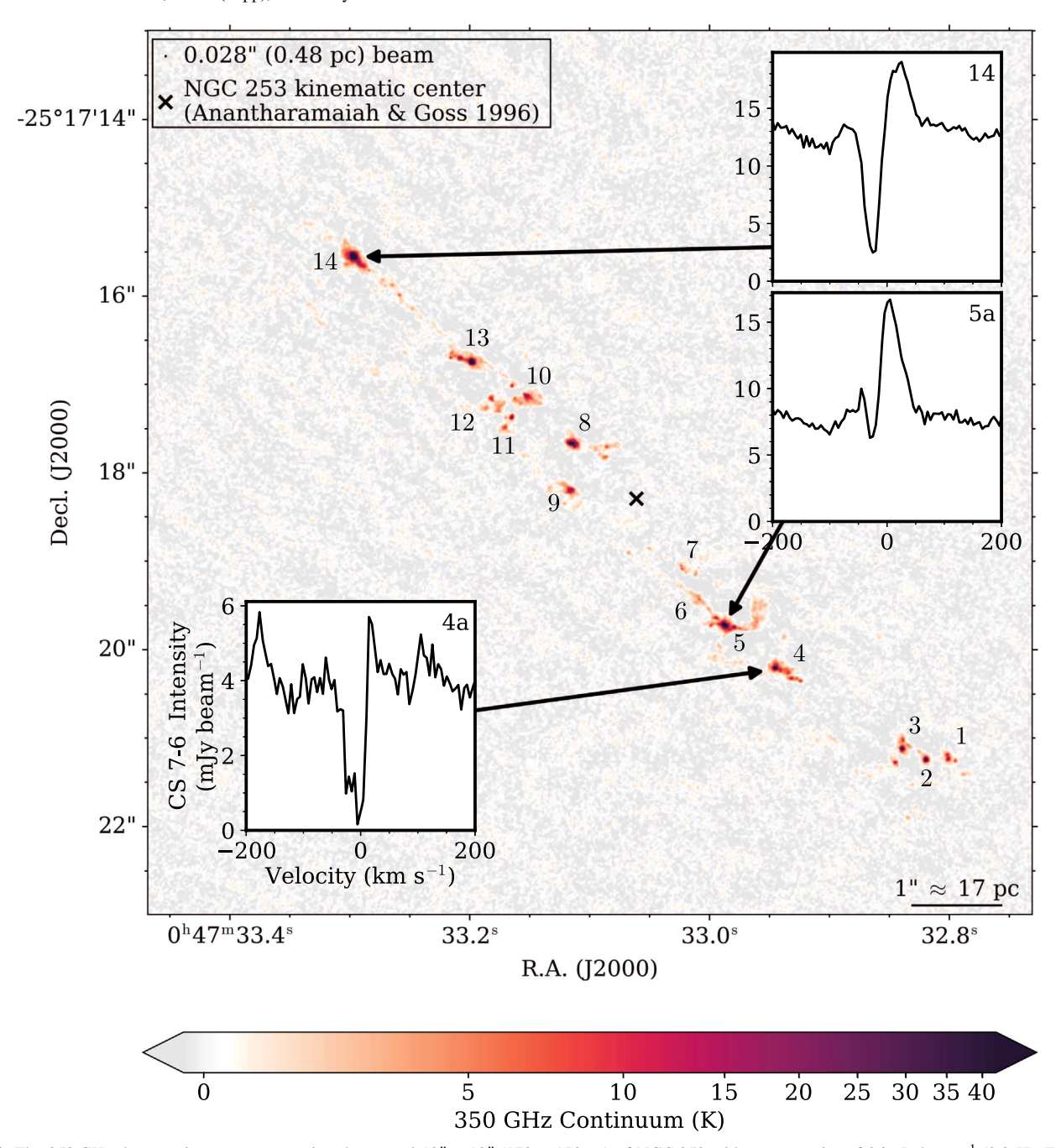


Figure 1. The 350 GHz dust continuum map covering the central $10'' \times 10''$ (170×170 pc) of NGC 253 with an rms noise of 26μ Jy beam⁻¹ (0.3 K). The beam FWHM is shown in the upper left corner. The × marks the center of NGC 253 from ionized gas kinematics traced by RRLs (Anantharamaiah & Goss 1996). The 14 clusters identified by Leroy et al. (2018) are labeled. Despite the increased resolution, most of the massive clusters identified by Leroy et al. (2018) persist, sometimes with a few lower-mass companion objects. The insets show the CS 7–6 spectra toward the three SSCs analyzed in this paper (SSCs 4a, 5a, and 14), highlighting the characteristic P-Cygni profiles indicative of outflows. These are the only clusters toward which we unambiguously identify blueshifted absorption signaling outflow activity.

supernova remnant, which is further supported by a non-negligible synchrotron component to this cluster's spectral energy distribution (SED; E. A. C. Mills et al. 2021, in preparation).

The position and orientation of each primary cluster is measured by fitting a 2D Gaussian to each cluster in the continuum image using emcee (Foreman–Mackey et al. 2013). The reported values are the medians of the marginalized posterior likelihood distributions (Table 1). As a nonparametric measurement of the cluster sizes, we compute the half-flux radius ($r_{half-flux}$) for each cluster. Given the cluster positions

and orientations from the 2D Gaussian fit, we construct elliptical annuli in steps of half the beam FWHM. The half-flux radius is the median of the cumulative flux distribution. We use this radius measurement as opposed to those from the 2D Gaussian fit because the cluster light profiles are not necessarily well described by a Gaussian, which will be discussed further in a forthcoming paper (R. C. Levy et al. 2021, in preparation). We deconvolve the beam from the radius measurements by removing half the beam FWHM from the half-flux radius in quadrature. The beam deconvolution will be treated more fully in a forthcoming paper focusing on the continuum properties of

Table 1
Primary Cluster Positions and Sizes Measured from the 350 GHz Continuum
Image

SSC Number	R.A. (J2000)	Decl. (J2000)	r _{half-flux} (pc)	$V_{\rm LSRK}$ (km s ⁻¹)
1a	0h47m32.801s	-25°17′21.236″	0.59	315
2	0h47m32.819s	$-25^{\circ}17'21.247''$	0.19	305
3a	$0^{h}47^{m}32.839^{s}$	-25°17′21.122″	0.47	302
4a	$0^{h}47^{m}32.945^{s}$	-25°17′20.209″	0.50	251
5a	$0^{h}47^{m}32.987^{s}$	-25°17′19.725″	0.76	215
7a	$0^{h}47^{m}33.022^{s}$	-25°17′19.086″	0.59	270
8a	$0^{h}47^{m}33.115^{s}$	$-25^{\circ}17'17.668''$	1.20	295
9a	$0^{h}47^{m}33.116^{s}$	-25°17′18.200″	0.46	155
10a	$0^{h}47^{m}33.152^{s}$	$-25^{\circ}17'17.134''$	1.32	280
11a	$0^{h}47^{m}33.165^{s}$	-25°17′17.376″	0.13	145
12a	$0^{h}47^{m}33.182^{s}$	-25°17′17.165″	1.29	160
13a	$0^{h}47^{m}33.198^{s}$	-25°17′16.750″	0.36	245
14	$0^{h}47^{m}33.297^{s}$	-25°17′15.558″	0.53	205

Note. The cluster positions and sizes for the primary SSCs identified from the 350 GHz continuum image (Figure 1). We follow the cluster naming convention of Leroy et al. (2018). Clusters that break apart into multiple subclusters have an "a" added to their number. We remove SSC 6 as it is likely not a true cluster due to its morphology. Positions are determined by fitting a 2D Gaussian. $r_{\rm half-flux}$ is the half-flux radius determined from the radial profile. The beam $(0.028'' = 0.48~\rm pc)$ has been deconvolved from the reported sizes. $V_{\rm LSRK}$ is the cluster systemic velocity (see Section 2.5). For SSCs 4a, 5a, and 14, the estimated uncertainty is $\pm 1~\rm km~s^{-1}$. For the other clusters, estimated uncertainties are $\pm 5~\rm km~s^{-1}$.

the SSCs, which will also include the lower resolution data (R. C. Levy et al. 2021, in preparation).

2.2. Imaging the Lines

We image the CS 7-6 and $H^{13}CN$ 4-3 lines by selecting a 800 km s⁻¹ window around the line center (rest frequencies of 342.883 and 349.339 GHz, respectively), assuming a systemic velocity of 243 km s⁻¹ (Koribalski et al. 2004). We clean the lines of interest using tclean in CASA version 5.4.1 with specmode='cube', deconvolver='multiscale', scales=[0], Briggs weighting with robust=0.5, and no uv-taper. No clean mask was used. The baseline was fit with a linear function (nterms=2) to account for any change in slope over the wide band. The continuum is not removed from the visibilities or the cleaned cubes. The cell (pixel) size is 0.0046" (0.078 pc), so that we place around 4 pixels across the minor axis of the beam. The final elliptical beam is $0.027'' \times 0.019''$. Finally, we convolve to a circular 0.028" (0.48 pc) beam. The rms noise is 0.5 mJy beam⁻¹ (6.5 K) per 5 km s⁻¹ channel. Figure 2 shows the peak intensity maps for CS 7–6 and H¹³CN 4-3 within ± 200 km s⁻¹ about the galaxy's systemic velocity to avoid possible contamination by other strong lines (especially by HC_3N in the case of $H^{13}CN$ 4–3).

2.3. Full Band Spectra and Detected Lines

Though the analysis is focused on the CS 7–6 and $H^{13}CN$ 4–3 lines, we also make a "dirty" cube covering the entire band and imaged area by running tclean with niter=0. This dirty cube has a cell (pixel) size of 0.02″ and an rms noise away from the emitting regions of 0.57 mJy beam⁻¹ per 5 km s⁻¹ channel. The synthesized beam is $0.05'' \times 0.025''$. The continuum is not removed from the visibilities or the dirty cube.

In Figure 3, we show the full band spectrum of SSCs 4a, 5a, and 14, extracted from the dirty cube and averaged over the FWHM continuum source size. There are several immediately striking features in these spectra. The brightest lines in SSCs 4a, 5a, and 14 show deep, blueshifted absorption features, extending down to ~ 0 mJy beam⁻¹, and redshifted emission. This line shape is commonly referred to as a P-Cygni profile—for the star in which it was first detected—and is indicative of outflows. As a comparison, we also show the spectrum of SSC 8a in Figure 3, which does not have these P-Cygni line shapes. We note that the CO 3–2 line has a complicated structure, likely because it traces lower density gas than other detected lines $(n_{\rm crit} \sim 2 \times 10^4 \, {\rm cm}^{-3}; {\rm e.g.}$, Turner et al. 2017) and so it arises in many places along the line of sight to the SSCs.

There are many detected lines in addition to the usual dense gas tracers. These include shock tracers such as SO 8–7 and SO₂ lines and vibrationally excited HC₃N and HCN 4–3, which are primarily excited through IR pumping (e.g., Ziurys & Turner 1986; Krieger et al. 2020). Many of these have been previously identified by Krieger et al. (2020), some of which are marked in Figure 3.

2.4. Correcting for Foreground Gas

Because the SSCs are embedded in the nucleus of NGC 253, there is dense gas along the line of sight that may contribute to the observed spectra but is not associated with the SSCs themselves. This can be seen in the line channel maps around each SSC, shown in Figure 4 for CS 7-6. This gas is most evident in SSCs 5a and 14, which both show changes in the gas morphology with velocity (relative to the cluster systemic velocity; see Section 2.5). The first panel of each set of channel maps shows the CO 3-2 velocity field in the same region as a tracer of the bulk gas motions not associated with the clusters themselves. Because we are interested in the large-scale gas motions, we smooth the CO 3-2 velocity maps presented by Krieger et al. (2019) to $5 \times$ the beam major axis $(5 \times 0.17'' = 0.85'' = 14.4 \text{ pc})$. The velocities shown in Figure 4 are relative to the cluster systemic velocities. All three clusters are located at different velocities compared to the bulk gas motions (i.e., CO 3-2 velocity maps are not centered on zero). In the case of SSC 14, the distinct morphological evolution with velocity matches qualitatively with the CO 3-2, though there is a velocity offset. It is difficult to know what fraction of this is associated with the clusters themselves or with dense gas in the environment of the clusters but not necessarily bound to them. Here, we will assume that all of the emission in the green annuli in Figure 4 is not bound to the clusters and should be corrected to obtain the intrinsic spectrum of the clusters. The spectrum of the environmental gas (T_{env}) is averaged in an annulus with an inner radius of $3\times$ the half-flux radius and an outer radius of $5 \times$ the half-flux radius, as shown in Figure 4. This effectively assumes the environmental dense gas forms a uniform screen in between the cluster and our line of sight. This is unlikely to be the case and is one of the uncertainties of this correction.

We calculate the optical depth (τ_{ν}) of the environmental gas following Mangum & Shirley (2015). Combining their Equations (24) and (27), we have

$$\tau_{\nu} = -\ln\left[1 - \frac{kT_{\text{env}}}{h\nu} \left(\frac{1}{e^{h\nu/kT_{\text{ex}}} - 1} - \frac{1}{e^{h\nu/kT_{\text{bg}}} - 1}\right)^{-1}\right], (1)$$

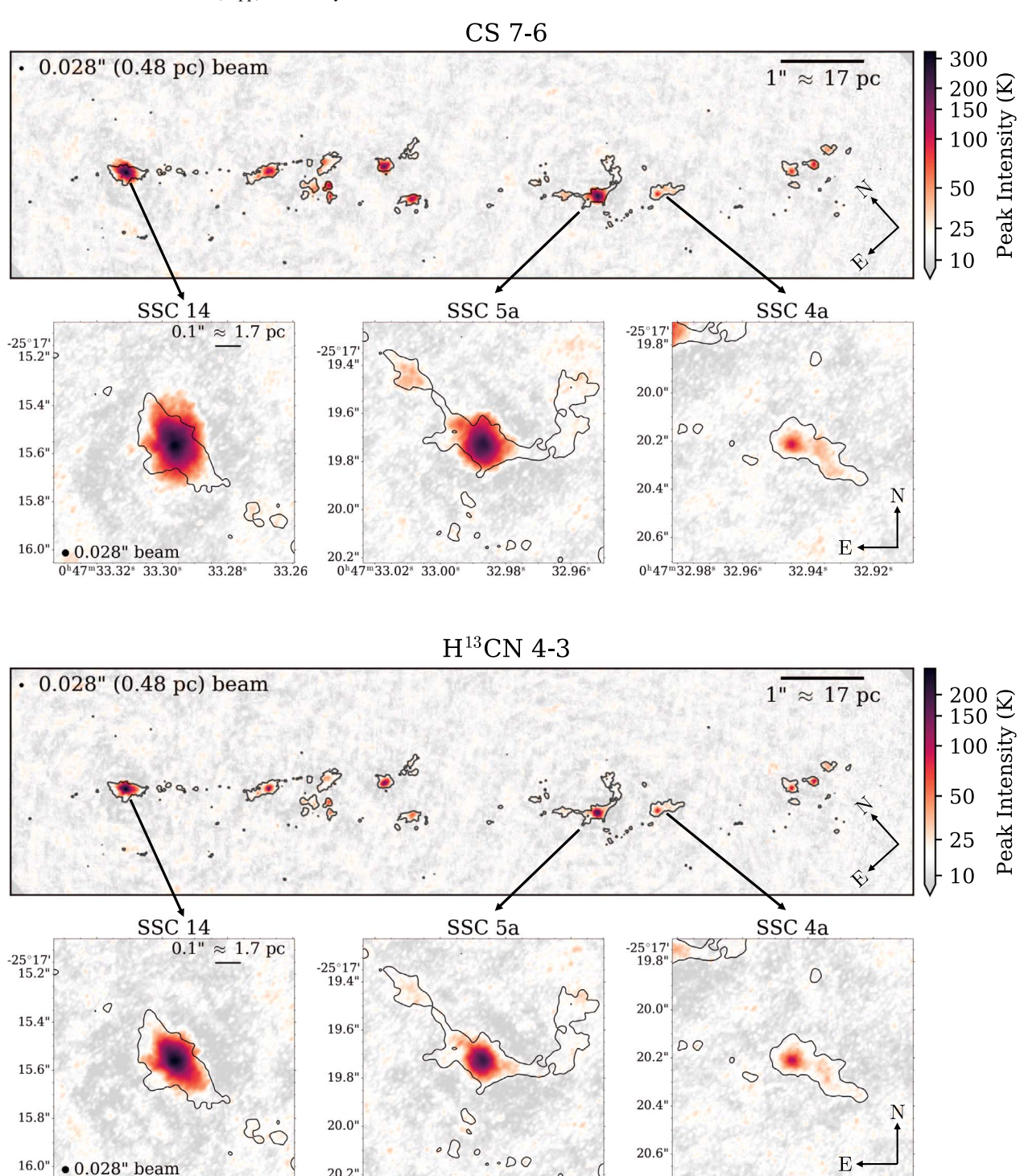


Figure 2. Peak intensity maps of CS 7-6 (top group) and H^{13} CN 4-3 (bottom group) within \pm 200 km s⁻¹ of the galaxy systemic velocity to avoid contamination by other strong lines in the band. The top panels in each group have been rotated so the linear structure is horizontal, as indicated by the coordinate axes in the lower right corner. The contours show $5\times$ the rms noise level in the 350 GHz dust continuum shown in Figure 1 ($5\times$ rms = 1.5 K), and so indicate the extent of the dust structures around the SSCs. The square plots show the peak intensity maps and dust continuum contours zoomed in to 1'' (17 pc) square regions around SSCs 14, 5a, and 4a, highlighting the localized and spatially resolved emission toward these SSCs. These have not been rotated, as indicated by the coordinate axes in the lower right corner.

32.98

32.96

0h47m32.98s 32.96s

where the filling fraction is assumed to be unity, the excitation temperature $(T_{\rm ex})$ is 102 ± 28 K, and the background temperature $(T_{\rm bg})$ is measured from the continuum level of the environmental spectrum (but is ≈ 0 K; Figure 5). The assumed value of $T_{\rm ex}$ is the average of the excitation temperatures found by Meier et al. (2015) over larger

33.28

33.26

0h47m33.02s 33.00s

0h47m33.32s 33.30

scales in the nucleus (74 K) and by Krieger et al. (2020) for regions more localized to the SSCs (130 K), since the true value of the excitation temperature of this dense gas near the clusters likely falls somewhere between these two measurements. The uncertainty reflects half of the difference of these two values.

32.94

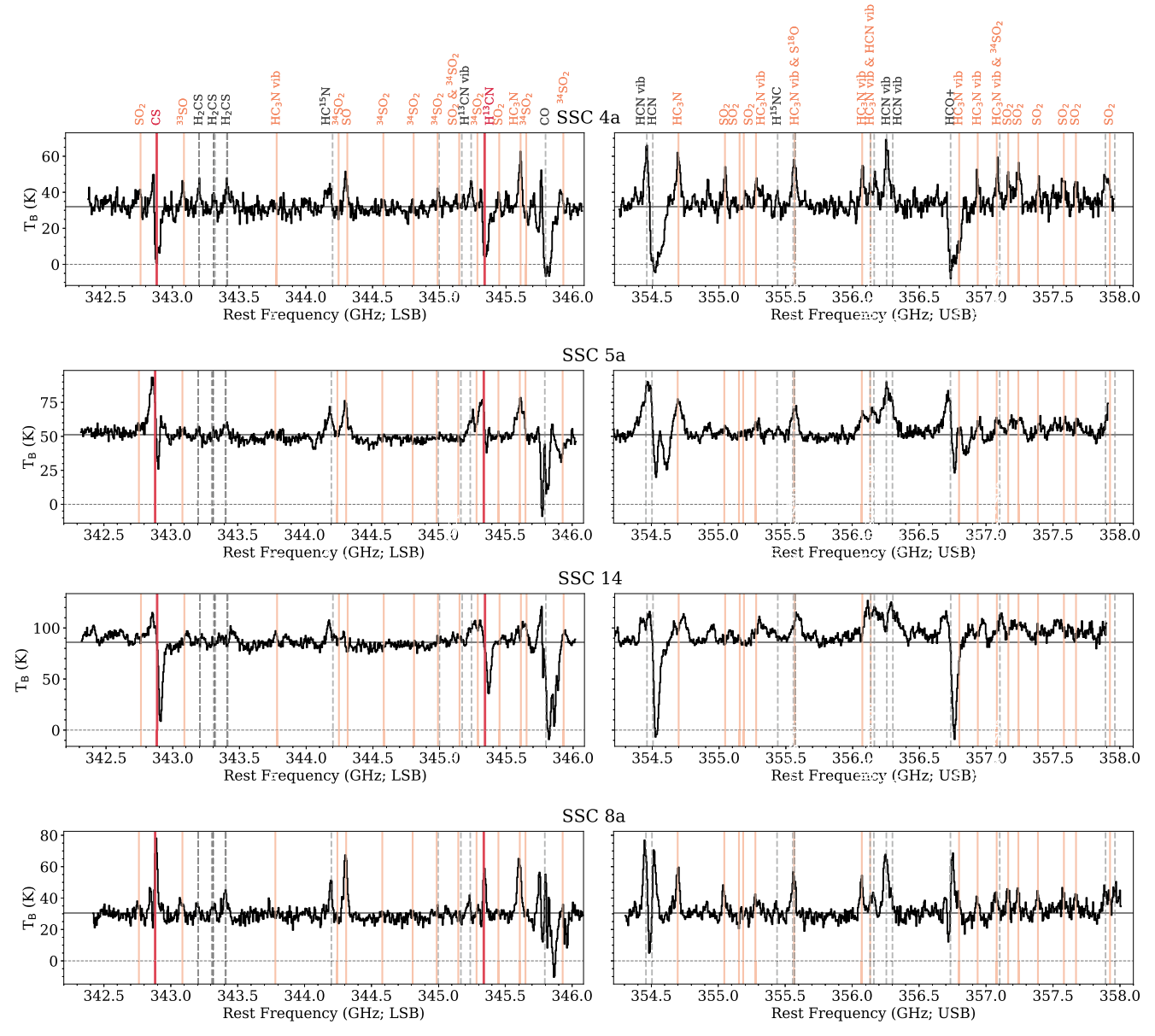


Figure 3. The full band spectra of SSCs 4a (top), 5a (top-middle), 14 (bottom-middle), and 8a (bottom). These spectra are averaged over the FWHM continuum source size and have been corrected for foreground gas (Section 2.4). The continuum has not been removed, and is shown by the solid horizontal gray lines. There are many spectral lines detected in these clusters, some of which are marked by the vertical lines and labels (where vib denotes a rovibrational transition; see also Krieger et al. 2020). The main lines used in this study (CS 7–6 and H¹³CN 4–3) are marked in red (thick solid), lines used to determine the systemic velocity are in orange (thin solid), and other lines are in gray (dashed). The P-Cygni profile is seen in many lines in SSCs 4a, 5a, and 14. In some cases, the absorption is saturated (i.e., absorbed down to zero intensity shown by the horizontal gray dashed lines) especially in the brightest lines (such as CO 3–2, HCN 4–3, and HCO⁺ 4–3). The CO 3–2 line profile is further complicated due to clouds along the line of sight. SSC 8a is shown as an example of bright source without evidence for outflows, though there may be a hint of inflows in CS 7–6, H¹³CN 4–3, and HCO⁺ 4–3.

We assume that half of the environmental emission comes from the foreground, so that the optical depth of the material along the line of sight in front of the cluster is $\tau_{\nu,fg} = \tau_{\nu}/2$. We also assume that the environmental gas is colder than the gas in the cluster, so it will absorb emission from the cluster. We then derive the corrected (intrinsic) SSC spectra

$$T_{\text{obs}} = T_{\text{intrinsic}} e^{-\tau_{\nu,fg}} + T_{\text{env}} (1 - e^{-\tau_{\nu,fg}})$$

$$\Rightarrow T_{\text{intrinsic}} = e^{\tau_{\nu,fg}} [T_{\text{obs}} - T_{\text{env}} (1 - e^{-\tau_{\nu,fg}})],$$
(2)

where the second equation is a rearrangement of the first. The observed, environmental, and intrinsic spectra of CS 7–6 for SSCs 4a, 5a, and 14 are shown in Figure 5. This process is repeated for $\rm H^{13}CN~4-3$ and the full band spectra in Figure 3.

As discussed earlier, it is difficult to determine what fraction of the extended emission seen in the channel maps (Figure 4) is environmental or associated with the cluster. Moreover, our method for the foreground correction is quite simplistic, and there are uncertainties related to the fraction of gas that may be associated with the clusters, the geometry of the environmental material, and the assumed excitation temperature. As can be seen in Figure 5, however, the correction mostly affects the peak of the emission components. After the foreground correction, the emission peak for SSC 14 increases by 7% (17 K), whereas the absorption trough only increases by 4.5% (1.5 K). There is no appreciable change in the spectra for SSCs 4a and 5a. The absorption features are, therefore, largely

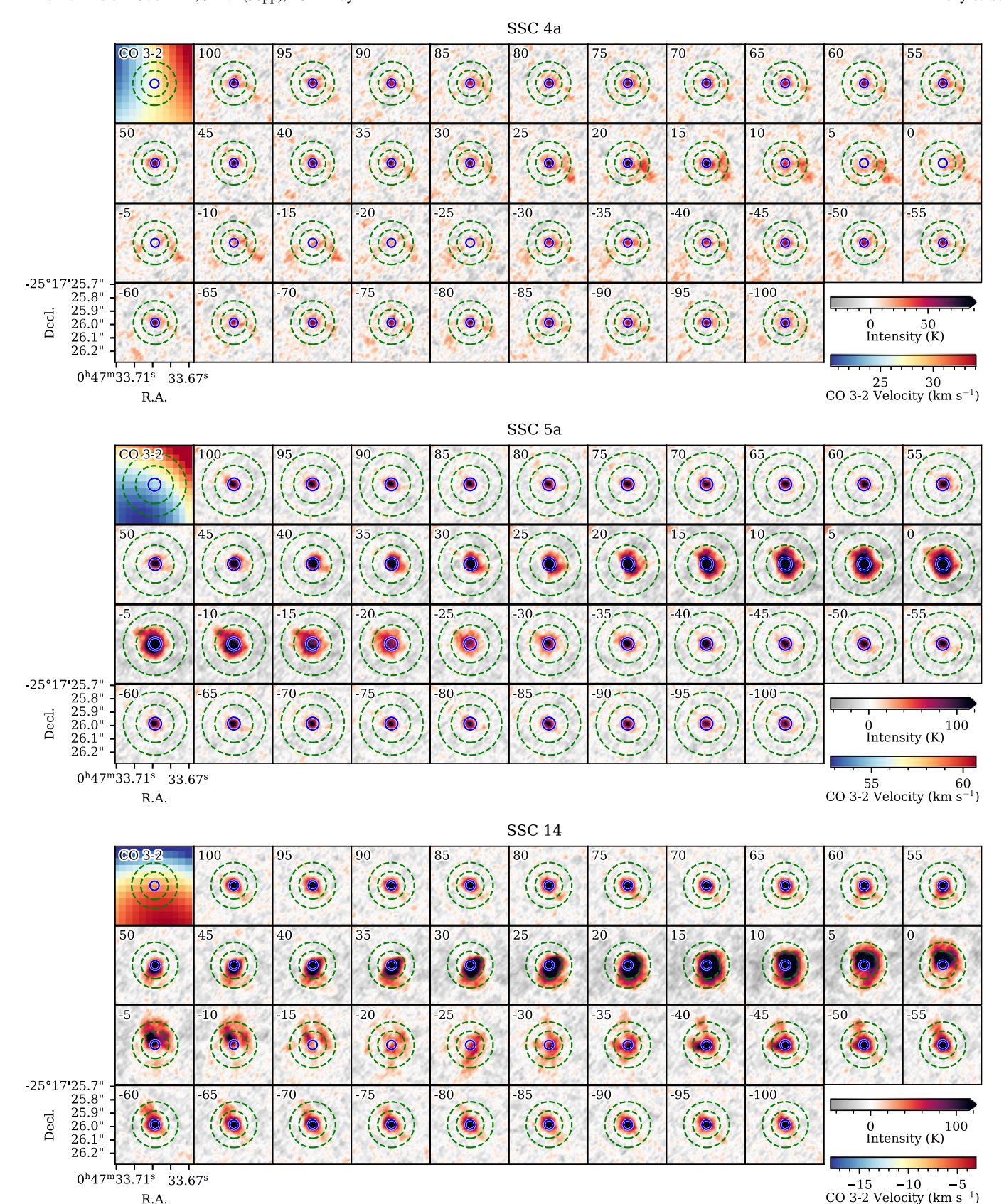


Figure 4. Channel maps around CS 7–6 for SSCs 4a (top), 5a (middle), and 14 (bottom) in $10 \text{ pc} \times 10 \text{ pc}$ regions. The continuum has not been removed. The first panel shows the smoothed CO 3–2 velocity field in this region (Krieger et al. 2019), indicative of the large-scale bulk gas motions. The CO 3–2 color scale and the labeled CS 7–6 velocity channels (in km s⁻¹) are relative to the cluster systemic velocity (Table 1). The solid blue circles show the continuum source sizes, and the green dashed annuli show the regions used for the foreground correction. The H¹³CN 4–3 channel maps are similar.

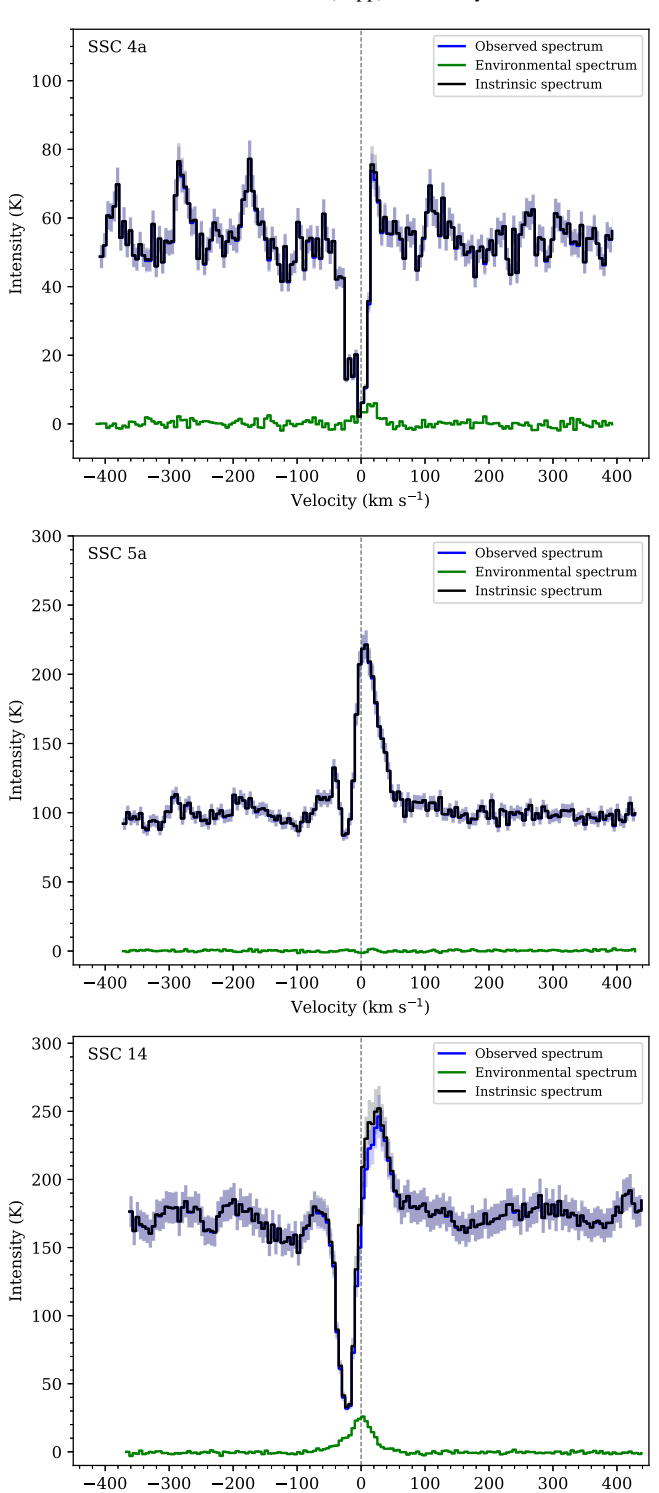


Figure 5. The CS 7–6 spectra for SSCs 4a (top), 5a (middle), and 14 (bottom) averaged over the 350 GHz continuum source area (blue; corresponding to the blue ellipses in Figure 4), the foreground gas (green; corresponding to the green annuli in Figure 4), and the corrected, intrinsic CS 7–6 spectrum accounting for the foreground gas (black). The blue shaded region around the observed spectrum reflects the standard deviation of the spectrum within the continuum source area. The gray shaded region around the intrinsic spectrum includes the propagated uncertainties from the assumed excitation temperature $(T_{\rm ex}=102\pm28~{\rm K})$. See Section 2.4 for details of the foreground gas correction.

Velocity (km s⁻¹)

unaffected by this correction, and the derived properties of the outflow (presented in Sections 3.1 and 3.2) are robust. The intrinsic (corrected) spectra are used throughout the analysis of this paper.

2.5. Cluster Systemic Velocities

We constrain the systemic velocity of all of the detected clusters using the full band spectra and the detected line list presented by Krieger et al. (2020). Using the full band spectrum for each cluster, we simultaneously fit each line in the line list using a series of Gaussians of the form

$$I(\nu) = I_{\text{cont}} + \sum_{\text{line}} I_{\text{line}} \exp\left[\frac{-(\nu - \nu_{\text{line-rest}})^2}{2\sigma_{\text{line}}^2}\right], \quad (3)$$

where I_{cont} is the fitted continuum level over the whole spectrum, I_{line} is the fitted intensity of each line, $\nu_{\text{line-rest}}$ is the fixed rest frequency of each line, σ_{line} is the fitted width of each line, and ν is the rest frequency of the observed spectrum, which depends on the assumed systemic velocity. The primary lines used to determine the systemic velocity are marked in orange in Figure 3; these lines tend to have strong emission and simple line shapes. Other strong lines in the band (e.g., CO 3-2, HCN 4-3, HCO $^+4-3$) tend to have complicated line shapes that make accurately determining the systemic velocity difficult. Due to the presence of lines with complicated shapes and line blending, the cross correlation of each full band spectrum and the multi-Gaussian fit is done by eye. The systemic velocities of for all the clusters are listed in Table 1. The uncertainty is estimated to be $\pm 5 \,\mathrm{km \, s^{-1}}$. For SSCs 4a, 5a, and 14, the systemic velocities are further refined and confirmed using other lines in the cleaned CS 7-6 and $\mathrm{H}^{13}\mathrm{CN}$ 4–3 cubes (Figure 6). Several of these lines—the vibrational transitions, in particular—have sharp peaks and are spatially localized to the clusters themselves. They, therefore, provide tighter constraints on the cluster systemic velocities. For SSCs 4a, 5a, and 14, we estimate that our cluster systemic velocities are accurate to $\pm 1 \text{ km s}^{-1}$.

2.6. Other Cluster Properties

In addition to cluster properties derived from these new 0.5 pc resolution data described in the previous subsections, we use stellar masses, total H_2 gas masses, and escape velocities of the clusters calculated by Leroy et al. (2018). Here, we briefly describe how these quantities were derived. These quantities are reproduced in Table 2 for the three clusters that are the focus of this work.

Stellar Masses (M_*)—The stellar masses are calculated based on the 36 GHz image from the Very Large Array (VLA) convolved to 0.11" (1.9 pc) resolution (Gorski et al. 2017, 2019; Leroy et al. 2018). At 36 GHz, the emission is assumed to be entirely due to free–free (Bremsstrahlung) emission. From the 36 GHz luminosity, Leroy et al. (2018) derived M_* for a zeroage main sequence (ZAMS) population with a standard initial mass function (IMF; see their Section 4.3.1 and Table 2). As described below, we consider additional sources of uncertainty beyond those described by Leroy et al. (2018). First, we assume

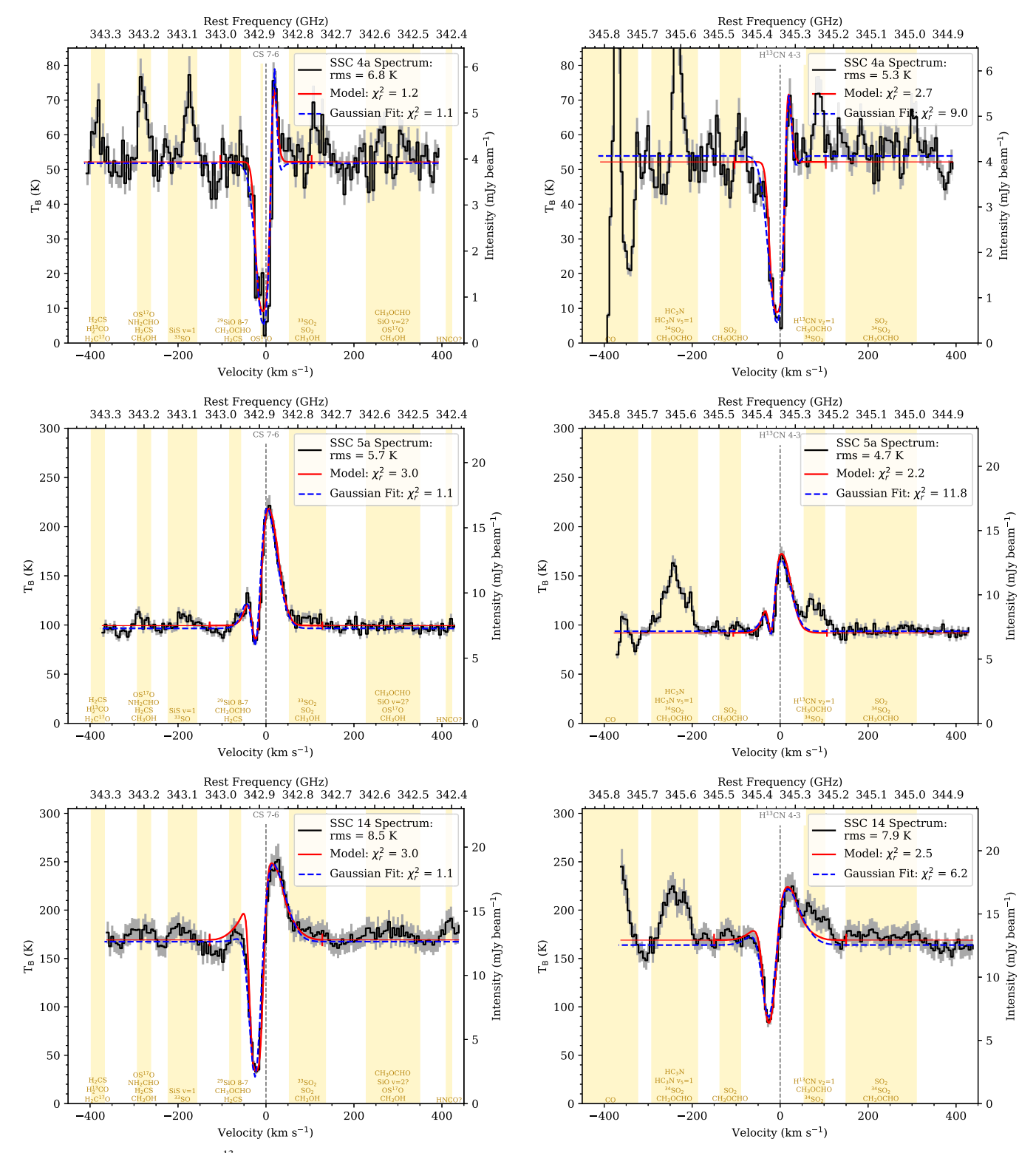


Figure 6. The CS 7–6 (left) and H¹³CN 4–3 (right) spectra for SSCs 4a (top), 5a (middle), and 14 (bottom). The yellow shaded regions show where other lines may contaminate the spectrum. Possible candidate lines are listed at the bottom of the yellow shaded regions. The blue dashed curves show the two-component Gaussian fit to the profile (Section 3.1). The solid red curves show the best-fitting spherical outflow models (Section 3.2). The vertical red line segments shows the range of velocities actually modeled, and the red curve outside of these vertical line segments is an extrapolation.

that the primary clusters retain all of the stellar mass measured by Leroy et al. (2018), which may lead to an overestimate of M_{\ast} for those clusters that break apart. We estimate that this is at worst 50% in those cases (although the higher resolution data presented here shows a number of satellite structures, the

original one remains dominant in most). Second, Leroy et al. (2018) estimated that there is a $\pm 20\%$ systematic uncertainty due to assumptions about the Gaunt factor. Finally, E. A. C. Mills et al. (2021, in preparation) measured the M_* of these clusters at 5 pc resolution using hydrogen RRLs. These agree with the M_*

 Table 2

 Cluster and Outflow Properties from Absorption Line Fits

Quantity	Unit	SSC 4a		SSC 5a		SSC 14	
		CS 7-6	H ¹³ CN 4-3	CS 7-6	H ¹³ CN 4-3	CS 7-6	H ¹³ CN 4-3
$\log_{10}(M_{\rm H_2,tot})^{\rm a}$	$\log_{10}(M_{\odot})$	5.1		5.3		5.7	
$\log_{10}(M_*)^{b}$	$\log_{10}(M_{\odot})$	5.0		5.4		5.5	
$V_{\rm escape}$	${\rm km~s}^{-1}$	22.0		33.2		45.5	
$ au^{ ext{d}}$		2.3	2.3	0.2	0.0	1.8	0.6
$V_{\text{max -abs}}$ e	$\mathrm{km}~\mathrm{s}^{-1}$	6	6	22	20	24	24
$V_{\text{out,max}}$ f	${\rm km}~{\rm s}^{-1}$	40	46	42	34	51	56
$\Delta V_{ m out,FWHM}$ g	${\rm km}~{\rm s}^{-1}$	40	46	24	17	32	38
$\log_{10}(t_{\rm cross})^{\rm h}$	$log_{10}(yr)$	5.0	5.0	4.5	4.6	4.4	4.4
$\log_{10}(N_{\rm H_2,out})^{\rm i}$	$\log_{10}(\text{cm}^{-2})$	23.9	25.3	22.7	23.2	23.7	24.6
$\log_{10}(M_{\rm H_2,out})^{\rm j}$	$\log_{10}(M_{\odot})$	4.7	6.1	3.8	4.3	4.6	5.5
$\log_{10}(M_{\rm H_2,out}/M_{\rm H_2,tot})^{\rm k}$		-0.4	1.0	-1.5	-1.0	-1.1	-0.2
$\log_{10}(M_{\rm H_2,out}/M_*)^{\rm k}$		-0.3	1.1	-1.6	-1.1	-0.9	-0.0
$\log_{10}(\dot{M}_{\rm H_2,out})^{-1}$	$\log_{10}(M_{\odot} \text{ yr}^{-1})$	-0.3	1.1	-0.7	-0.3	0.2	1.1
$\log_{10}(t_{\text{remove-gas}})^{\text{m}}$	$log_{10}(yr)$	5.4	4.0	6.0	5.6	5.5	4.6
$\log_{10}(p_{\rm r}/M_{*})^{\rm n}$	$\log_{10}(\text{km s}^{-1})$	0.7	2.1	0.0	0.5	0.7	1.6
$\log_{10}(E_{\rm kin})^{\rm o}$	$\log_{10}(erg)$	49.2	50.6	49.6	49.9	50.4	51.3

Note. Values (aside from the top three) are derived from fits to the absorption component of the line profiles. See Section 3.1 and Appendix A for details on how these values were calculated.

estimated by Leroy et al. (2018) to within ± 0.3 dex on average. For SSCs 4a, 5a, and 14, the agreement is even better, and the RRL analysis finds M_* , which differ by ± 0.1 , ± 0.1 , and ± 0.2 dex from those derived from the 36 GHz emission, where ± 0.1 means the RRL measurements produce a larger (smaller) ± 0.1 means the calculations by E. A. C. Mills et al. (2021, in preparation) is the effect of a synchrotron component. If synchrotron contaminates the 36 GHz flux (which is assumed to be entirely free-free in the ± 0.1 means the RRL measurements produce a larger (smaller) ± 0.1 means

12a; E. A. C. Mills et al. 2021, in preparation). To determine the lower error bar on M_* , we take the largest of the above three sources of uncertainty for each cluster, where the uncertainty from the RRL measurements are included only if they yield a smaller M_* . To determine the upper error bars, we take the larger of the 20% systematic uncertainty and RRL-measured M_* where they yield a larger M_* . In addition to these quantifiable uncertainties on M_* , there are unquantified uncertainties relating to ionizing photons absorbed by dust and evolution beyond the ZAMS, both of which would result in the reported stellar masses being underestimates (Leroy et al. 2018). While we do not attempt to calculate these unquantifiable uncertainties, we caution that they could be important. In this work, we use these

^a The cluster gas mass measured from the dust continuum and assuming a gas-to-dust ratio of 100 (Leroy et al. 2018). Uncertainties are \sim 0.4–0.5 dex, with these measurements likely biased low due to assumptions about the dust temperature, dust-to-gas ratio, and the dust opacity. See Section 2.6 for a detailed discussion of how these values were calculated

^b The cluster zero age main-sequence (ZAMS) stellar mass measured from the 36 GHz free–free emission (Leroy et al. 2018). See Section 2.6 for a detailed discussion of the uncertainties on these stellar masses.

^c The escape velocity from the cluster (Leroy et al. 2018). Uncertainties are dominated by those from the gas and stellar masses. See Section 2.6 for a detailed discussion of how these values were calculated.

 $^{^{\}mathrm{d}}$ The optical depth in the outflow calculated from the absorption to continuum ratio (Equation (A4)).

^e The velocity where the absorption is maximized, corresponding to the velocity at which the bulk of the material traced by CS 7–6 and H¹³CN 4–3 is outflowing. ^f The maximum outflow velocity, defined as 2σ from the mean outflow velocity (Equation (A3)). For a Gaussian line, this means that 95% of the dense material has an outflow velocity slower than $V_{\text{max out}}$.

g The FWHM line width from the Gaussian fit to the absorption feature.

^h The gas crossing time, or the time it would take a parcel of gas to travel from the center of the cluster to r_{SSC} at $V_{max-abs}$ (Equation (A2)).

ⁱ The H_2 column density in the outflow derived from τ (Equations (A5)–(A9)). This calculation assumes local thermal equilibrium (LTE) with an excitation temperature of 130 ± 56 K and abundances of CS 7–6 and H^{13} CN 4–3 relative to H_2 from Martín et al. (2006). The abundances may vary by an order of magnitude on these small scales, so all quantities that depend on the column density are limited to order-of-magnitude precision. The blueshifted outflow component only probes the portion of the outflow on the approaching side, so the values are multiplied by two to account for the receding side of the outflow, assuming it is identical to the approaching side. Uncertainties are ± 1 dex.

^j The H₂ mass in the outflow derived from $N_{\rm H_2}$, out and the projected cluster size (Equation (A10)). This calculation and others that depend on it assume the outflow is spherical, which is supported by the results of our modeling (Section 3.2). Uncertainties are ± 1 dex.

^k The H₂ mass in the outflow compared to the total gas or stellar mass in the cluster. Uncertainties are ± 1 dex.

¹ The mass outflow rate derived over one crossing time (Equation (A11)). Uncertainties are ± 1 dex.

^m The gas-removal time, or the time it would take for the current mass outflow rate to expel all of the cluster gas mass $(M_{\rm H_2}, \, {\rm tot})$ from the clusters (Equation (A12)). Uncertainties are $\pm 1 {\rm dex}$.

 $^{^{}n}$ The radial momentum carried by the outflow per unit stellar mass, which also assumes the outflow is spherical (Equation (A13)). Uncertainties are ± 1 dex.

 $^{^{}m o}$ The kinetic energy of the outflow calculated from $M_{
m H_2}$, out and $V_{
m max\,-abs}$ (Equation (A14)). Uncertainties are ± 1 dex.

stellar masses primarily to place the clusters in a mass-radius diagram and to evaluate the possible mechanisms powering the observed outflows.

Total H_2 Gas Mass $(M_{\rm H_2}, \text{ tot})$ —The cluster gas masses are based on the 350 GHz image from ALMA at 0.11" (1.9 pc) resolution (Leroy et al. 2018). At 350 GHz, the majority of the emission is due to thermal dust emission, though there may be a small level of free-free contamination. Leroy et al. (2018) quantified this free-free contamination and corrected the measured 350 GHz fluxes to determine a more accurate flux due to thermal dust emission (see their Section 4.1 and Table 1). Assuming a dust temperature of 130 K, dust-to-gas ratio of 1:100, and a dust mass absorption coefficient of $1.9 \text{ cm}^2 \text{ g}^{-1}$, Leroy et al. (2018) calculated the total H_2 mass of the clusters. Uncertainties are $\sim 0.4-0.5$ dex, with these measurements likely biased low due to assumptions about the dust temperature, dust-to-gas ratio, and the dust opacity. See their Section 4.3.3 and Table 2 for more details. In this work, we consider these to be the total gas masses of the clusters, including gas still bound within the cluster and outflowing from it.

Escape Velocity ($V_{\rm escape}$)—Leroy et al. (2018) calculated the escape velocity from the clusters using their measured stellar and gas masses and their measured sizes from Gaussian fits to the 0.11" (1.9 pc) resolution 350 GHz image. Uncertainties are dominated by those from M_* and $M_{\rm H_2}$, tot. See Section 4.3.6 and Table 2 of Leroy et al. (2018) for more details. In this work, we use these escape velocities to compare against the outflow velocities we measure to place constraints on whether the outflowing material will escape the cluster.

2.7. Outflow Candidates

We analyze the spectra toward all of the clusters (primary or otherwise) identified in the high-resolution continuum data (Figure 1) in search of spectral outflow signatures. We determine our final list of outflow candidates based on robust detections of blueshifted absorption and redshifted emission in the CS 7–6 and $\rm H^{13}CN$ 4–3 lines. We present SSCs 4a, 5a, and 14 as our conservative list of detected P-Cygni profiles indicative of outflows. The CS 7–6 and $\rm H^{13}CN$ 4–3 spectra toward SSCs 4a, 5a, and 14 are shown in Figure 6, which are from the cleaned line cubes (Section 2.2) and have been corrected for foreground gas (Section 2.4).

While other SSCs show absorption features, they are not due to outflowing material as the absorption occurs at the line center. Absorption at the line center is likely due to self-absorption of the cold material surrounding the cluster against the embedded continuum source(s). Redshifted absorption would be indicative of material inflowing toward the cluster; a hint of inflow is perhaps seen toward SSC 8a (Figure 3, especially the CS 7–6, HCN 4–3, and HCO⁺ 4–3 lines). Blueshifted absorption, on the other hand, means that the cold foreground material is outflowing from the cluster. For this analysis, we are focused on the blueshifted absorption indicative of outflows.

We also verify that these absorption features are not induced by the spatial filtering by the interferometer. Due to the incomplete sampling of the Fourier plane and the lack of short spacings, emission on larger scales is filtered out and cannot be properly deconvolved, causing an increase in the rms of the data at the velocities where bright extended emission would be present. This problem manifests itself as negative "bowls" around bright emission, but also as negative features that have velocity structure. While this mainly affects the continuum (which is not removed from these data), it can also induce false absorption features in the affected velocity range. This can be seen, for example, in the CO 3–2 lines in Figure 3, where the absorption profiles are very complex. Our choice to focus on CS 7–6 and H¹³CN 4–3 mitigates this problem, as these transitions require high densities to be excited and are hence fairly localized to the clusters themselves, with not much of an extended component. As shown in Figure 5, the environmental CS 7–6 spectra around the SSCs are either flat or show the line in emission; the H¹³CN 4–3 spectra show similar profiles. Therefore, we conclude that the CS 7–6 and H¹³CN 4–3 absorption features are not a result of the spatial filtering by the interferometer, although it may contribute to uncertainties at the 10% level.

A careful measurement of the cluster systemic velocities (Section 2.5) is critical to determine whether the absorption is blueshifted with respect to the cluster or not. Critically, for a few clusters (e.g., SSCs 3a and 13a) there are pathological combinations of absorption at the line center coupled with strong vibrationally excited lines in emission at the redshifted edge of the absorption feature, which together could masquerade as P-Cygni profiles. We identify other line candidates present in the spectra around CS 7-6 and H¹³CN 4-3 using the line list presented by Krieger et al. (2020) as well as Splatalogue, 14 which are listed in the yellow shaded regions in Figure 6. It is outside the scope of this paper to verify precisely which other lines are present in the spectra, so we present them simply as possible candidates (or combinations of candidates), which confuse the CS 7-6 and H13CN 4-3 spectra. This line blending can lead to false detections of P-Cygni profiles. For example, $H^{13}CN 4-3 v_2 = 1$ is located 100 MHz (\approx 88 km s⁻¹) redward of H¹³CN 4–3, as can be seen in the right column of Figure 6. Similarly, HCN $4-3 v_2 = 1$ is located only 45 MHz (\approx 38 km s⁻¹) redward of HCN 4-3. Given the broad line profiles (in emission and absorption), these lines can easily blend together to produce a facsimile of a P-Cygni profile. A careful measurement of the cluster systemic velocities (using other lines with simpler profiles), cross referencing with the line list presented by Krieger et al. (2020), and further verification using Splatalogue (see footnote 14) reveals that these are not true P-Cygni profiles. It is also worth noting that there is an emission feature (likely OS¹⁸O, an SO₂ isotopologue) seen in the CS 7-6 absorption trough of SSC 4a (upper left panel of Figure 6).

That we detect outflows from SSCs 4a, 5a, and 14 is in large part due to our ability to spatially resolve the individual clusters, since the spectral signatures of the outflows are localized roughly to the central half-flux radius of the clusters. In retrospect, there are indications of these outflows in the CS 7 -6 and H^{13} CN 4-3 line profiles presented by Leroy et al. (2018, see their Figure 3) in SSCs 4 and 14. The much weaker outflow in SSC 5a is not apparent in these lower resolution data where the clusters are only marginally resolved. There are also kinematic offsets between HCN 4-3 and $H40\alpha$ measurements toward these clusters which are consistent with the effects of these outflows at lower resolution (E. A. C. Mills et al. 2021, in preparation).

¹⁴ https://www.cv.nrao.edu/php/splat/advanced.php

2.8. Internal Cluster Kinematics

Here, we briefly investigate whether SSCs 4a, 5a, and 14 exhibit signs of internal rotation. Observational detections of rotation in star and globular clusters in the Milky Way are mixed (e.g., Kamann et al. 2019; Cordoni et al. 2020), though simulations predict that massive star clusters (>1000 M_{\odot}) should have appreciable rotation (Mapelli 2017).

We investigate the internal kinematics by constructing position—velocity (PV) diagrams over a range of angles as well as peak-velocity and intensity-weighted velocity (moment 1) maps around each of the clusters. While we see no clear signs of internal rotation, the absorption hinders this analysis significantly as it affects the (effective) intensity weighting of the peak- and intensity-weighted velocity (moment 1) maps. It similarly confuses the interpretation of the PV diagrams. Therefore, we cannot claim that the SSCs are not rotating, only that, given the presence of absorption, we see no clear evidence for rotation. We also check clusters without absorption or outflow signatures, and also find no evidence of rotation.

3. Results

Using ALMA data at 350 GHz at 1.9 pc resolution, Leroy et al. (2018) identified 14 marginally resolved clumps of dust emission whose properties are consistent with forming SSCs. In our new 0.5 pc resolution data, many of these SSCs fragment substantially such that there is a bright, massive primary cluster surrounded by smaller satellite clusters (Figure 1). From the 0.5 pc resolution 350 GHz dust continuum image (Figure 1), we identify roughly three dozen clumps of dust emission. We spectrally identify candidate outflows toward three SSCs: SSCs 4a, 5a, and 14 (where the appended "a" denotes the primary cluster of the fragmented group). The locations of these clusters within the nucleus of NGC 253 are shown in Figure 1, where the insets show the CS 7-6 line profiles toward these three clusters. In each of these SSCs, we see evidence for blueshifted absorption and redshifted emission in many lines (Figure 3), but we focus on the CS 7-6 and $H^{13}CN$ 4-3 lines (Figure 6), which provide the best balance between bright lines with sufficient S/N, absorption features that do not suffer from saturation effects, and that probe gas localized to the clusters. This line shape—blueshifted absorption and redshifted emission—is commonly referred to as a P-Cygni profile and is indicative of outflows.

We take two approaches to derive the physical properties of the outflows in each cluster. First, we fit the absorption component of the line profiles to measure the outflow velocity, column density, mass, mass outflow rate, momentum, etc. (Section 3.1). Second, we model line profiles of the CS 7–6 and H¹³CN 4–3 spectra toward each cluster with the goal of constraining the outflow opening angles and orientations to the line of sight (Section 3.2). While the primary goal of the line profile modeling is to constrain the outflow geometry, it also provides a measurement of the outflow velocity, column density, mass, mass outflow rate, etc. We compare common parameters of these methods in Section 3.3 and discuss our recommended values in Section 3.4.

3.1. Outflow Properties from Absorption Line Fits

For a first estimate, we measure the outflow velocities, column densities, gas masses, and momentum of each outflow by fitting the profiles of $\rm H^{13}CN~4{-}3$ and $\rm CS~7{-}6$ with a two-

component Gaussian (blue dashed curves in Figure 6). We exclude the portions of the spectra that may be contaminated by other lines, as marked by the yellow shaded regions in Figure 6. The fit to the absorption feature yields the velocity at the maximum absorption ($V_{\text{max-abs}}$), or the velocity at which the bulk of the material is outflowing. We define the maximum outflow velocity as 2σ from the average velocity ($V_{\rm max,out} \equiv V_{\rm max\,-abs} + 2\frac{\Delta V_{\rm out,FWHM}}{2.355}$), which means that 95% of the material traced by CS 7–6 and H¹³CN 4–3 has an outflow velocity slower than $V_{\text{max,out}}$ (for a truly Gaussian line). Given the mean outflow velocity and the cluster size, we calculate the crossing time, or the time for a parcel of gas to travel from the center of the cluster to the edge $(t_{\rm cross} \equiv r_{\rm SSC}/V_{\rm max-abs})$, where r_{SSC} is equivalent to the half-flux radius (Table 1). From the fitted absorption to continuum intensity ratio, we derive the optical depth and hence the column density in absorption. We convert from the column density of the molecule to H₂ $(N_{\rm H}, \text{ out})$ using abundances from Martín et al. (2006). From the column density and projected size (Table 1), we estimate the H_2 mass in the outflow (M_{H_2} , out) assuming the outflow is spherical. Constraints on the opening angle of the outflows derived from modeling of the line profiles are discussed in Section 3.2 and show that the outflows must be nearly spherical. Given the mass, crossing time, and mean outflow velocity, we calculate the mass outflow rate ($\dot{M}_{\rm H_2,out}$), the gasremoval timescale ($t_{\text{remove-gas}}$), the radial momentum injected per unit stellar mass in the cluster (p_r/M_*) , and the kinetic energy of the outflow $(E_{\rm kin})$. Further details and equations used to derive these quantities are presented in Appendix A. The outflow parameters derived from the absorption profile fits are reported in Table 2.

The clusters have outflows with maximum velocities $(V_{\rm max,out})$ of $\sim 40-50\,{\rm km\,s}^{-1}$. For all three SSCs with outflows, $V_{\rm max,out}$ is larger than the escape velocity ($V_{\rm escape}$; reproduced in Table 2 from Leroy et al. 2018 and see also Section 2.6). The bulk of the material traced by CS 7-6 and H¹³CN 4-3, however, has velocities less than $V_{\rm escape}$ (as traced by $V_{\rm max-abs}$). For SSCs 4a, 5a, and 14, 20%, 7%, and 7% of the outflowing material has velocities larger than the escape velocity and will be able to escape from the cluster. Gas that is outflowing with velocities below $V_{\rm escape}$ may be reaccreted by the cluster. The gas crossing time ($t_{\rm cross}$) is $\sim {\rm few} \times 10^4$ yr, which is a lower limit on the age of the outflow. These timescales and the possibility of reaccretion will be discussed further in Section 4.1.

The masses in the outflows are large. The molecular hydrogen column densities and masses derived from H¹³CN 4-3 are larger than those derived from CS 7-6 in all cases. One possibility is that CS 7-6 is more optically thick than $H^{13}CN$ 4–3, which may be supported by the depth of the absorption in SSC 4a, but this cannot explain the discrepancy in SSC 5a. A more likely possibility is that the relative molecular abundances we assume are not correct for these small, extreme regions. We adopt molecular abundances for $H^{13}CN$ and CS with respect to H_2 of $[H^{13}CN]/[H_2] =$ $(1.2 \pm 0.2) \times 10^{-10}$ and $[CS]/[H_2] = (5.0 \pm 0.6) \times 10^{-9}$ from a study of the the center of NGC 253 at 14"-19" $(\sim 240-320 \,\mathrm{pc})$ resolution by Martín et al. (2006), where the brackets refer to the abundance of that species. Adopting these abundances on the parsec scales of our clusters, however, is highly uncertain. Observations of envelopes around high-mass young stellar objects in the Milky Way, for example, reveal

order-of-magnitude variations in the abundances of molecules, especially nitrogen and sulfur bearing species (van Dishoeck & Blake 1998, and references therein). The impact of the uncertainty on the fractional molecular abundances is that they translate into order-of-magnitude accuracy for the H₂ column density measurements, as well as the subsequent calculations, which depend on the column density, as reported in Table 2. In the following subsection we discuss in more detail what we know about chemical abundances and their variation: our conclusion is that the masses derived from H¹³CN 4–3 are likely more accurate.

3.1.1. Fractional Abundance Variations

To resolve the discrepancies between our abundancedependent measurements ($N_{\rm H_2}$, out, $M_{\rm H_2}$, out, $\dot{M}_{\rm H_2,out}$, and $t_{\rm remove-gas}$) from CS 7–6 and H¹³CN 4–3 would require that either [CS]/[H₂] is enhanced and/or [H¹³CN]/[H₂] is reduced in these clusters compared to the values measured by Martín et al. (2006). In the case of CS, modeling by Charnley (1997) shows that [CS]/[H₂] varies from $\sim 10^{-10}$ – 10^{-8} depending on age, O2 abundance, and temperature, with CS being most abundant after $\sim 10^4$ yr, at low O₂ abundance and at low temperatures ($T \sim 100 \text{ K}$), though the trend with temperature is not monotonic. Estimates of the kinetic temperatures of the (marginally resolved) clusters vary from ~200-300 K (Rico-Villas et al. 2020). At $\sim 10^5$ yr (the ZAMS ages of these clusters; Rico-Villas et al. 2020) and a temperature of 300 K, Charnley (1997) found [CS]/[H₂] $\sim 4 \times 10^{-9}$ depending on the assumed temperature and O₂ abundance, very close to our assumed ratio of $(5.0 \pm 0.6) \times 10^{-9}$ measured by Martín et al. (2006). From CS, SO, and SO₂ line ratios toward these clusters, Krieger et al. (2020) suggested that [CS]/[H₂] may be enhanced by a factor of 2-3 from the values measured by Martín et al. (2006). For SSCs 5a and 14, an enhancement of [CS]/[H₂] by a factor of 2–3 brings our abundance-dependent measurements into much better agreement with those derived from $H^{13}CN$ 4–3, but this is not sufficient for SSC 4a. The gas in SSC 4a is likely more optically thick than in SSCs 5a and 14, as seen in the absorption to lower temperatures (\sim 7 K), which could help explain the lingering discrepancy in this cluster.

In the case of [H¹³CN]/[H₂], Colzi et al. (2018) found that chemical evolution does not affect nitrogen fractionation, so the main driver of a different [H¹³CN]/[H₂] in these SSCs would be due to changes in the $^{12}\text{C}/^{13}\text{C}$ ratio. If there is less ^{13}C in these clusters compared to the environment, then [H¹³CN]/[H₂] may be lower. Toward these clusters, Krieger et al. (2020) found hints that $^{12}\text{C}/^{13}\text{C}$ may be on the high side of the assumed ratio of 40 ± 20 (Martín et al. 2010, 2019; Henkel et al. 2014; Tang et al. 2019). If the the ^{12}C abundance remains the same, this suggests that reductions in ^{13}C and hence [H¹³CN]/[H₂] are possible. To bring our abundance-dependent measurements from H¹³CN 4–3 into agreement with the lower values derived from CS 7–6 would imply $^{12}\text{C}/^{13}\text{C} \gtrsim 300$, much larger than even the highest ratios measured in NGC 253 (Martín et al. 2010) while keeping ^{12}C fixed. Changing [H¹³CN]/[H₂], therefore, likely plays a minor role in remedying the differences in our abundance-dependent quantities.

If, therefore, the discrepancy between our abundance-dependent quantities measured from CS 7–6 and H¹³CN 4–3 is due to a change in the abundances of those species, the effect is likely driven by CS, which is enhanced relative to our

assumed [CS]/[H₂] with perhaps a small contribution from reduced [H¹³CN]/[H₂]. As a result, the abundance-dependent quantities derived from H¹³CN 4–3 are likely more accurate. In the values presented here and in the following section, we adopt the abundances measured by Martı́n et al. (2006) and maintain the conservative order-of-magnitude uncertainties on these quantities.

3.2. Outflow Properties from Line Profile Modeling

The short gas crossing times, large outflow masses, and outflow mass rates (Table 2) suggest the outflow activity in these objects cannot be sustained for a long time. From this standpoint, it is reasonable that we detect outflows in $\lesssim 10\%$ of the SSCs, so it is possible that we are indeed catching a small fraction of the SSCs in this short-lived phase. The analysis in Section 3.1, however, implicitly assumes that the outflows are spherical. Another possibility, however, is that the outflows are biconical with a more-or-less narrow opening angle. In that case the outflows from the three clusters we identify are serendipitously pointed close enough to the line of sight to make them detectable. If the observed outflows are not spherical, geometric correction factors will need to be applied to the measured quantities in Table 2, and more outflows could exist that we do not detect because their geometry is unfavorable.

In order to determine whether the observed outflows are spherical or biconical and how they are oriented with respect to the line of sight, we build a simple radiative transfer model to model the spectrum through the outflow. 15 We consider spherical and biconical outflows, where the opening angle (θ) and orientation to the line of sight (Ψ) of the biconical outflows can be varied. Opening angles are defined as the full angle for one hemisphere; the maximum opening angle is $\theta = 180^{\circ}$, corresponding to a sphere. Technical details and equations are presented in Appendix B, but we summarize the basic scheme here. We construct a four-dimensional box (x, y, z, ν) , where radii are measured in spherical coordinates from the center of the box. We define the measured cluster radius such that $r_{\rm SSC} = r_{\rm half-flux}$ (Table 1). The simulated box is scaled to $4 \times r_{\rm SSC}$ in each spatial dimension (x, y, z) to fully encompass the line emission (e.g., Figure 4) especially since the geometry along the line of sight (z-axis) is unknown. The velocity axis is scaled based on the input outflow velocity and velocity dispersion, so that the velocity resolution is optimized over the velocities relevant for the cluster and outflow; this is described more fully in Appendix B. Three physical components are required to adequately model the CS 7–6 and H¹³CN 4–3 spectra, as shown in Figures 7 and 8. These components and the input parameters for each are described below. The input parameters are denoted with table footnote "a" in Table 3, which lists input parameter values that yield the best model fits. Radial profiles of these components and the input parameters are summarized in Figure B2 in Appendix B.

1. Dust continuum component: Shown in green in Figures 7 and 8, this component is a sphere with $r = r_{\rm SSC}$ and a constant (in space and frequency) temperature ($T_{\rm cont}$). The optical depth in a single cell is a maximum ($\tau_{\rm cont,max}$) at the center, then decreases like a Gaussian with FWHM = $2 \times r_{\rm SSC}$. In other words, the FWHM of the

 $[\]overline{^{15}}$ The code and best-fit input parameter files are available at https://github.com/rclevy/ModelSSCOutflows.

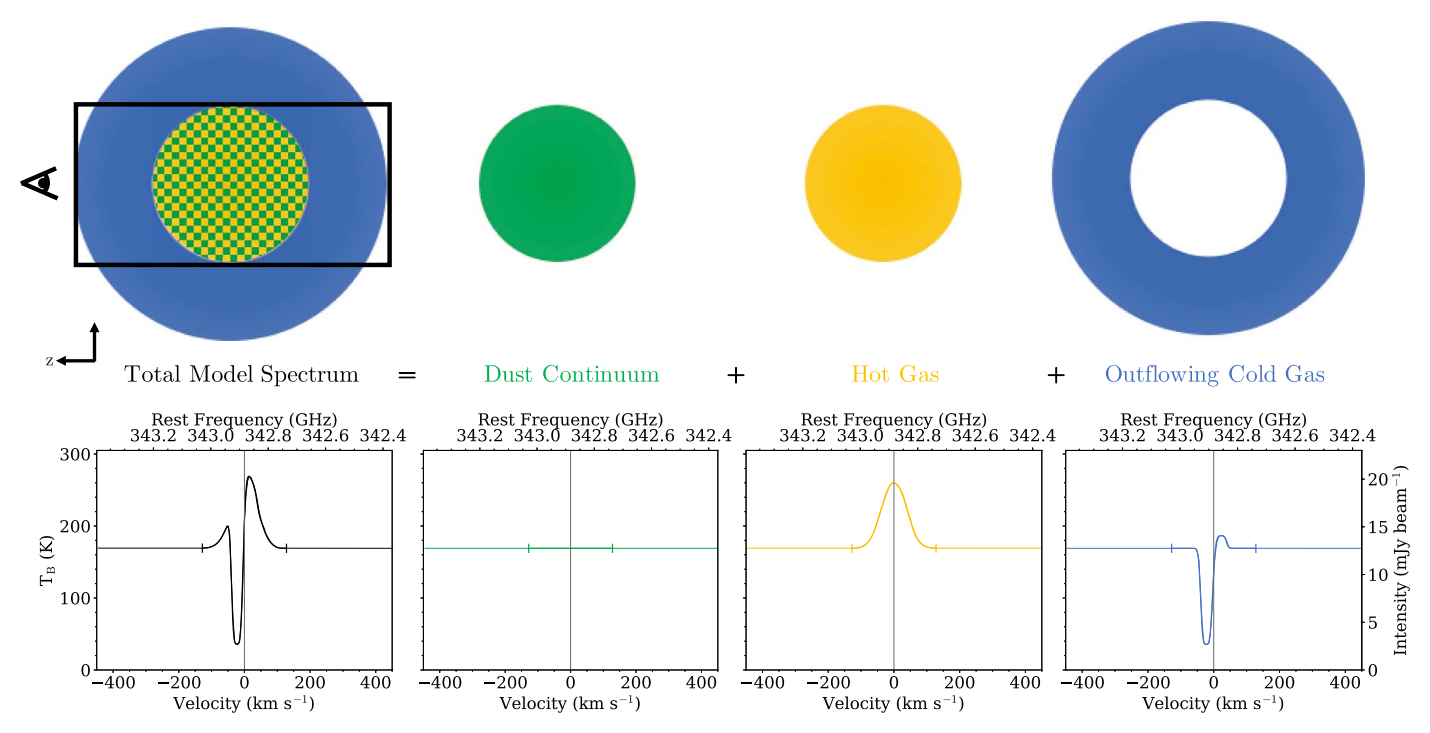


Figure 7. A 2D schematic showing the three physical components of the model at a slice through the box at x = 0 and their spectral contributions. The black rectangle shows the slice of the field of view used to calculate the final spectrum. A representative spectrum for each component is shown below the corresponding 2D schematic. CS 7–6 toward SSC 14 is used here as an example. The thicker curves bounded by the vertical line segments show the velocity range modeled, whereas the thin curves outside are an extrapolation. The hot gas and cold outflowing gas spectra include the dust continuum component so that the absorption due to the outflowing components is visible.

dust continuum optical depth profile matches the diameter of the 350 GHz continuum source. The temperature and optical depth are set to zero for $r > r_{\rm SSC}$.

- 2. Hot gas: Shown in yellow in Figure 7 (and encompassed within the green sphere in Figure 8), this spherical component is required to reproduce the strong emission component of the P-Cygni profiles. This component is defined by an input hot gas temperature (T_{hot}) , a H_2 volume density (n_{hot}) for the central (r=0) pixel, and a velocity dispersion $(\Delta V_{\text{hot,FWHM}})$. T_{hot} is constant (spatially) for $r \leq r_{\text{SSC}}$, and is set to zero outside. The density falls off $\propto r^{-2}$ from the center and is set to zero for $r > r_{\text{SSC}}$. The line is centered on zero velocity along the frequency axis, and the Gaussian line width is given by $\Delta V_{\text{hot,FWHM}}$. Using the equations in Appendix B, this produces a spectrum at every pixel in the box.
- 3. Cold, outflowing gas: Shown in blue in Figures 7 and 8, this is the outflow component that produces the absorption features. This component is defined by an input gas temperature (T_{out}) , a H₂ volume density (n_{out}) at the cluster boundary $(r = r_{SSC})$, a constant outflow velocity (V_{out}), a velocity dispersion ($\Delta V_{\text{out,FWHM}}$), an opening angle (θ) , and an orientation to the line of sight (Ψ) . The gas temperature is constant (spatially) within this component. The density is a maximum at $r = r_{SSC}$ and deceases $\propto r^{-2}$ until the edges of the box; the density is set to zero inside the cluster $(r < r_{SSC})$. In the spectral dimension, the line has a centroid velocity given by $V_{\rm out}$ and an FWHM line width of $\Delta V_{\rm out,FWHM}$. Using the equations in Appendix B, this produces a spectrum at every pixel in the box. Since the outflow velocity is constant and the density $\propto r^{-2}$, the outflow conserves mass, energy, and momentum. To create a biconical

outflow with the input opening angle (θ) , the velocity of the pixels outside the outflow cones is set to zero. This creates an ambient gas component (shown in light blue in Figure 8), which has the same temperature, density, and velocity dispersion properties as the outflowing gas (but with $V_{\rm out}=0$). The box is then rotated to the input orientation from the line of sight (Ψ) .

Together, these three components are integrated from the back of the box forward (e.g., along the -z-axis in Figures 7 and 8). To obtain the final spectrum, only pixels within a cylinder along the line of sight with $r = r_{SSC}$ are integrated (shown as the black cylinder in Figure 8) to best compare with the measured spectra, which are extracted only over an area corresponding to the continuum source half-flux radius. We adjust the input parameters component-by-component to find the model spectrum that best matches the observed CS 7-6and H¹³CN 4-3 spectra for SSCs 4a, 5a, and 14. There are degeneracies among input parameters, which are described below and in Appendix B. These best-fit models are shown in red in Figure 6, and the best-fit parameters for CS 7-6 and H¹³CN 4–3 are listed in Table 3. For all spectra and sources, the spherical model provides the best fit, implying that the opening angles of the outflows need to be broad to explain the observed line profiles. A wide opening angle is in agreement with recent magnetohydrodynamic simulations, which show that cluster outflows are asymmetric and chaotic, but still wide angle in general and regardless of the precise feedback mechanism (e.g., Skinner & Ostriker 2015; Kim et al. 2018; He et al. 2019; Lancaster et al. 2021a, 2021b; Geen et al. 2021). From these best-fit models, we also calculate the H₂ column density and mass in the outflows, which are also listed in Table 3.

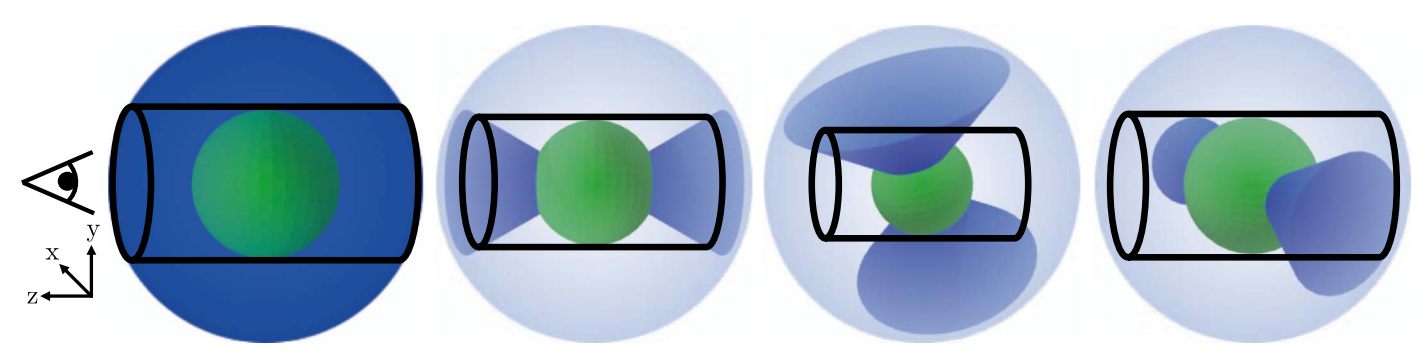


Figure 8. 3D schematics of (from left to right) a spherical ($\theta = 180^{\circ}$) outflow, a biconical ($\theta = 60^{\circ}$) outflow pointed along the line of sight, and biconical ($\theta = 90^{\circ}$ and $\theta = 45^{\circ}$) outflows that are inclined to the line of sight ($\Psi = 95^{\circ}$ and $\Psi = 60^{\circ}$). The green central sphere includes both the dust continuum and hot gas components and has $r = r_{SSC}$. The dark blue outer shell or cones show the outflowing gas. The light blue component shows the ambient gas between the outflow cones. The black cylinder shows the line of sight and field of view over which the model spectrum is integrated and averaged, which has $r = r_{SSC}$ (in the xy-plane) and spans $4 \times r_{SSC}$ along the z-axis.

We tested models with a fourth physical component representing a fast outflowing component. This was mainly motivated by SSC 14 and the mismatch between the spectrum and model at the blueward edge of the absorption feature for both CS 7–6 and H¹³CN 4–3 (Figure 6). In the model, this component is otherwise identical to the "slow" outflow component described above but with a larger outflow velocity and velocity dispersion and a different maximum H₂ volume. While including this component did marginally improve the fits —especially for SSC 14—the improvement was not enough to justify the additional three parameters introduced into the model.

Our model assumes a constant outflow velocity and r^{-2} density profile to conserve mass, energy, and momentum in the outflow. In reality, a constant outflow velocity is unlikely to be precisely the case, due to turbulence within the outflow itself (e.g., Raskutti et al. 2017) and because the outflow may decelerate as it encounters the surrounding medium. From the data, we investigate the location of the absorption trough around and across the sources. We see no strong evidence for systematic velocity shifts around or across SSCs 4a, 5a, or 14.

There are ranges of opening angles (θ) and orientations (Ψ) that are degenerate and will produce similar output spectra. To investigate how well we can constrain θ and Ψ , we run a grid of models with the same input parameters as in Table 2 with varying θ in steps of 20° and Ψ in steps of 5° . The results for CS 7–6 in SSC 14 are displayed in Figure 9, which shows that wide outflows and/or those pointed close to the line of sight are strongly favored. Wide-angle outflows from clusters are in agreement with the results of numerical simulations as mentioned previously. Though the outflows in simulations are clumpy and highly nonuniform, they cover nearly 4π steradians and hence approach the spherical limit of our simple modeling. Narrow and/or off-axis opening angles substantially increase the required input density in our models and result in unphysical solutions for the outflowing mass. In any case, we cannot pin down the precise opening angle and/or line-of-sight orientation from this modeling, but we place limits on them that suggest the dearth of clusters with observed outflows is not a selection bias due to geometrical effects. It is possible that we miss outflows if the dense gas is very optically thick and therefore obscures underlying outflow signatures (e.g., Aalto et al. 2019). We could also miss weak outflows below our detection limit of sensitivity and cluster mass.

3.3. Comparing the Two Methods

The two methods of measuring the outflow properties described have calculated quantities in common. In Figure 10, we compare the velocity where the absorption is maximum $(V_{\text{max-abs}})$, the FWHM of the absorption feature ($\Delta V_{\text{out,FWHM}}$), the maximum outflow velocity ($V_{\rm out,max}$), the gas crossing time $(t_{\rm cross})$, the H₂ column density in the outflow $(N_{\rm H_2}, {\rm out})$, the H₂ mass in the outflow $(M_{\rm H_2}, \, {\rm out})$, the mass outflow rate $(\dot{M}_{\rm H_2, out})$, and the time to remove all of the gas mass of the cluster at the current $\dot{M}_{\rm H_2,out}$ ($t_{\rm remove-gas}$). The equations used to calculate these parameters are given in Appendices A and B for the absorption line fits and line profile modeling, respectively. The vertical axis of Figure 10 shows the logarithm of the ratio of the quantities derived from each method; each major tick mark and horizontal grid line corresponds to an order-ofmagnitude difference. In general, there is good agreement between the two methods for the quantities that depend on the velocity of the outflow $(V_{\text{max-abs}}, \Delta V_{\text{out,FWHM}}, V_{\text{out,max}}, \text{ and})$ $t_{\rm cross}$). The uncertainties in Figure 10 reflect the adopted orderof-magnitude uncertainties around the abundance ratios, as discussed in Section 3.1.

Given the uncertainties the agreement between the absorption line fits and the line profile modeling is good, especially for H¹³CN 4–3. A notable exception is for CS 7–6 in SSC 4a, where the line profile modeling yields 1.5 dex larger H₂ columns and masses than derived from the absorption line fits. This is likely because the CS 7-6 absorption in SSC 4a is the most saturated (i.e., the closest to zero). For the absorption line fits, this renders a more uncertain optical depth (from the absorption to continuum ratio) as small changes in the absorption depth leads to large changes in the optical depth and hence the column density. For the line profile modeling, the depth of the absorption depends on the assumed gas temperature and H₂ volume density in the outflow. The bottom of the absorption trough sets an upper limit on the assumed gas temperature in the outflow (T_{out}) ; in the modeling, the temperature of the absorption trough cannot be lower than the assumed T_{out} . In the case of SSC 4a, this temperature is low $(\sim 7 \text{ K})$, well below the temperature needed to excite the J=7level of CS of 66 K (Schöier et al. 2005). ¹⁶ As a result, the H₂ density in the outflow must be increased, leading to a large outflowing mass. We assume a constant temperature in the

¹⁶ This information was retrieved from the Leiden Atomic and Molecular Database on 2020 October 30.

Table 3
Line Profile Modeling Input Parameters and Calculated Values

	Unit	SSC 4a		SSC 5a		SSC 14	
Quantity		CS 7 - 6	$H^{13}CN 4 - 3$	CS 7 - 6	$H^{13}CN 4 - 3$	CS 7 - 6	$H^{13}CN 4 - 3$
V _{max -abs} a,b	km s ⁻¹	7	7	25	22	25	28
$\Delta V_{\rm out,FWHM}$ a,c	$\mathrm{km}\ \mathrm{s}^{-1}$	25	25	20	15	20	25
$V_{ m out,max}$ d	${\rm km~s^{-1}}$	28	28	42	35	42	49
$\log_{10}(t_{\rm cross})^{\rm e}$	$log_{10}(yr)$	4.9	4.9	4.5	4.6	4.4	4.3
$\Delta V_{ m hot,FWHM}$ a,c $T_{ m out}$ a,f	${\rm km~s}^{-1}$	10	10	50	50	80	85
$T_{\text{out}}^{\text{a,f}}$	K	7	7	25	20	35	40
$T_{\text{hot}}^{\text{a,g}}$ $T_{\text{cont}}^{\text{a,h}}$	K	900	900	800	800	800	800
$T_{\rm cont}^{\rm a,h}$	K	105	105	200	185	340	340
$\log_{10}(n_{\text{out}})^{\text{a,i}}$	$\log_{10}(\text{cm}^{-3})$	7.8	7.5	5.5	5.9	6.2	6.8
$\log_{10}(n_{\text{hot}})^{\text{a,i}}$	$\log_{10}(\text{cm}^{-3})$	8.6	9.9	8.8	9.8	8.8	10.0
$\log_{10}(\tau_{\mathrm{cont,max}})^{\mathrm{a,j}}$		-1.3	-1.3	-1.3	-1.3	-1.3	-1.3
$\log_{10}(N_{\rm H_2,out})^{\rm k}$	$\log_{10}(\mathrm{cm}^{-2})$	25.4	25.1	23.2	23.7	24.0	24.5
$\log_{10}(M_{\rm H_2,out})^{\rm k}$	$\log_{10}(M_{\odot})$	6.3	6.0	4.4	4.9	5.3	5.4
$\log_{10}(\dot{M}_{\rm H2,out})^{\rm k}$	$\log_{10}(M_{\odot} \text{ yr}^{-1})$	1.4	1.1	-0.1	0.3	0.9	1.1
$\log_{10}(t_{\text{remove-gas}})^{\mathbf{k}}$	$log_{10}(yr)$	3.7	4.0	5.4	5.0	4.8	4.6

Notes. The input and output or derived parameters for the best-fitting spherical outflow models. See Section 3.2 and Appendix B for details.

outflowing gas, whereas a temperature gradient is likely needed to produce this absorption depth. Because the other sources and lines have shallower absorption depths, they do not suffer from this effect. Other strong lines-HCN 4-3 and HCO⁺ 4–3—shown in Figure 3 also suffer from this saturation, which is why they are not the focus of this analysis. We, therefore, suggest that the column density, mass, and mass outflow rate from the modeling are overestimated in the case of CS 7–6 in SSC 4a. This effect is not seen in the absorption line fitting because the absorption to continuum ratio is used to infer the optical depth, but an excitation temperature of 130 K is assumed to derive the level populations (Appendix A). In the line profile modeling, the input gas temperature (7 K in the case of CS 7-6 in SSC 4a) is used to derive the level populations instead (Appendix B). Discrepancies between the two methods are also seen in both lines toward SSC 5a, though they are not as extreme as for SSC 4a. The discrepancies in SSC 5a cannot, however, be explained by saturation. The same abundance ratios are used for both methods and these enter into the calculations in the same way, so this discrepancy cannot be remedied by changing $[CS]/[H_2]$.

3.4. Recommended Values

Given the number of assumptions of the line profile modeling and the parameter covariances, we suggest that the outflow properties from the absorption line fits presented in Table 2 are more reliable and should be adopted. The assumption of spherical outflows in computing those numbers is substantiated

by the modeling, which strongly favors wide outflows (Figure 9). It is encouraging that the line profile modeling generally finds similar values for the outflowing mass, but there are cases where the model likely overestimates the outflowing mass (e.g., SSC 4a). Both sets of measurements are limited in the same way by the uncertainty on the molecular abundances with respect the H₂. As discussed in Section 3.1.1, discrepancies between quantities derived from CS 7–6 and H¹³CN 4–3 may be driven primarily by changes in [CS]/[H₂] relative to the assumed abundance, so that quantities derived from H¹³CN 4–3 may be more reliable. Studies, such as the ALMA Comprehensive High-Resolution Extragalactic Molecular Inventory (ALCHEMI)¹⁷ that measure abundances at higher spatial resolution than currently available in these extreme environments may improve the accuracy of our column density, mass, mass outflow rate, and gas-removal timescale estimates.

4. Discussion

The existence of outflows in SSCs 4a, 5a, and 14 suggests these clusters may be in a different evolutionary stage compared to the other SSCs in the starburst. In the following section, we investigate the relationship between various timescales relevant to the clusters (Section 4.1) and possible outflow mechanisms (Section 4.2). We also investigate SSC 5a in more detail, as it is the only cluster visible in the NIR and

^a Best-fit input parameters to the model. The uncertainties listed below are reflective of the grid of tested parameters.

 $^{^{\}text{b}}$ The outflow velocity, which is assumed constant. Uncertainties are $\pm 1~\text{km s}^{-1}.$

^c The FWHM velocity dispersion of the given component. Uncertainties are ± 2 km s⁻¹.

^d The maximum outflow velocity defined as $V_{\text{max-abs}} + 2\frac{\Delta V_{\text{out,FWHM}}}{2.355}$. Propagated uncertainties are $\pm 2 \text{ km s}^{-1}$.

The gas crossing time defined as $\frac{r_{SSC}}{V_{max-abs}}$. Propagated uncertainties are 4% for SSCs 14 and 5 and 14% for SSC 4a.

f The gas temperature in the outflow at the line peak, which is constant spatially. Uncertainties are ± 2 K.

 $[^]g$ The gas temperature in the hot component at the line peak, which is constant spatially. Uncertainties are ± 25 K.

 $^{^{\}text{h}}$ The continuum temperature, which is constant spatially and spectrally. Uncertainties are $\pm 5~\text{K}.$

 $^{^{\}rm i}$ The log of the peak H_2 number density for the given component. Uncertainties are ± 0.25 dex.

^j The peak optical depth of the continuum component. Uncertainties are ± 0.025 .

 $^{^{}k}$ Uncertainties are ± 1 dex due to the molecular abundance ratios relative to H_{2} .

¹⁷ https://alchemi.nrao.edu

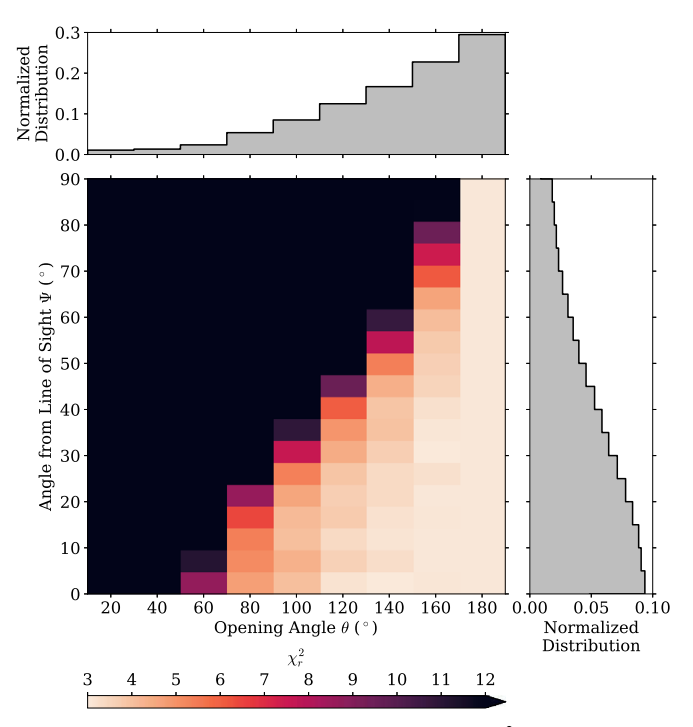


Figure 9. A heat map showing the reduced chi-squared (χ_r^2) values for models with varying opening angles (θ) and orientations from the line of sight (Ψ) for the same input parameters as listed in Table 3 for CS 7–6 in SSC 14. The gray histograms show the marginalized distributions for θ (top) and Ψ (right), normalized to unit area. This shows that the outflow opening angles must be wide and/or closely aligned with the line of sight.

shows evidence for a shell of dense gas surrounding it (Section 4.3).

4.1. Timescales, Ages, and Evolutionary Stages

There are several timescales and ages calculated from this and previous analyses for these clusters, which we summarize here and list in Table 4:

ZAMS Age ($t_{\rm ZAMS-age}$)—Rico-Villas et al. (2020) used the ratio of the luminosity in protostars to that of ionizing ZAMS stars to estimate the ages of the clusters ($t_{\rm ZAMS-age}$), finding that SSC 4a is $\sim 10^{4.95}$ yr old, SSC 5a is $\gtrsim 10^5$ yr old, and SSC 14 is $\sim 10^{4.88}$ yr old (Table 4). These measurements are based on the same 36 GHz emission used by Leroy et al. (2018) to calculate the stellar masses. The stellar masses and ages associated with the ionizing photon rates derived from the ZAMS assumption may be underestimated if the cluster stellar population has evolved beyond the ZAMS stage, or if some fraction of the ionizing photons are absorbed by dust. These three SSCs have negligible synchrotron components of their SEDs, so synchrotron contamination of the 36 GHz emission is a small effect. These ages are, therefore, likely lower limits on the true "age" of the cluster.

Cluster Formation Timescales—Given the $t_{\rm ZAMS-age}$ and freefall times ($t_{\rm ff}$) calculated by Leroy et al. (2018), we can try to place the clusters in a relative evolutionary sequence. An important caveat is that Leroy et al. (2018) estimated $t_{\rm ff}$ based on the marginally resolved data. With these spatially resolved data, the radii of the clusters decreased (e.g., Figure 11), meaning that these values of $t_{\rm ff}$ may be overestimated. SSCs 4a, 5a, and 14 have $t_{\rm ZAMS-age}/t_{\rm ff}=1.1$, \gtrsim 2.0, and 2.4, respectively (Table 4). Modeling by Skinner & Ostriker (2015) suggests that gas is actively collapsing to form stars on timescales \sim 1–2 $t_{\rm ff}$,

the typical timescale for cluster formation is $\sim 5t_{\rm ff}$, and the gas is completely dispersed by $\sim 8t_{\rm ff}$. These clusters should be nearing the end of the period of active gas collapse. SSC 5a may possibly be transitioning to the initial stages of gas dispersal, especially because it is the only cluster visible in the NIR (Section 4.3), though the gas dispersal has not yet finished because we still see evidence for an outflow. It is important to note, however, that these evolutionary stages are not clear-cut divisions, as gas accretion can continue while the cluster is forming and while outflows are present, and that the $t_{\rm ZAMS-age}$ are likely lower limits on the cluster ages. Moreover, the possibility that expelled gas is reaccreted onto the clusters may mean that this cluster formation sequence is more cyclic.

Crossing Time (t_{cross})—The crossing times (t_{cross}) we report in Tables 2 and 3 are short: $10^{4.5-5.2}$ yr. Similarly short crossing times are also seen in a SSC candidate in the Large Magellanic Cloud ($\sim 10^{4.8}$ yr; Nayak et al. 2019) and in simulations (e.g., Lancaster et al. 2021a, 2021b). At least one crossing time has passed since the outflows turned on, as P-Cygni line profiles are detected out to $\gtrsim r_{\rm SSC}$. If the outflows are present beyond $r_{\rm SSC}$, they are increasingly difficult to detect in absorption away from the continuum source. Therefore, this timescale places a lower limit on the age of the outflow.

Gas-removal Time ($t_{\rm remove-gas}$)—The gas-removal times ($t_{\rm remove-gas}$) are longer in general than the crossing or freefall times, though the uncertainties on $t_{\rm remove-gas}$ are large. The average $t_{\rm remove-gas} \sim 10^{5.0\pm0.6}$ yr, where the uncertainty is the standard deviation of the mean $t_{\rm remove-gas}$ for each SSC and line. The gas-removal times are $\gtrsim t_{\rm ZAMS-age}$, except for SSC 4a. Assuming a constant mass outflow rate, this would imply that there is still gas in the clusters to be removed, though a constant mass outflow rate is unlikely (e.g., Kim et al. 2018). This timescale also assumes that none of the expelled gas is reaccreted later on. Given that the bulk of the gas has outflow velocities below the escape velocity (Section 3.1), reaccretion of material is a likely scenario.

Gas Depletion Timescale (t_{dep}) —This timescale is the duration of future star formation, assuming a constant star formation rate (SFR) for each cluster and no mass loss: t_{dep} $\equiv M_{H_2,\text{tot}}/\text{SFR}$, where M_{H_2} , tot is from Leroy et al. (2018). The SFRs we use are also from Leroy et al. (2018) and are based on the measured 36 GHz fluxes that trace the free-free emission from each cluster (Gorski et al. 2017, 2019). This estimate of $t_{\rm dep}$ based on the SFR assumes continuous star formation (over \sim 10 Myr; Murphy et al. 2011), whereas we would expect the actual star formation in these clusters to be bursty. These are the longest timescales for each cluster listed in Table 4. Compared to the clusters' $t_{ZAMS-age}$, this may suggest that the clusters are early in their star formation process and that there is plenty of fuel to form new stars and for the clusters to continue grow. This assumes, however, that all of the molecular gas remains in the cluster. The current gas-removal times of the outflows ($t_{\text{remove-gas}}$) are much shorter than t_{dep} , indicating that these outflows will substantially affect the cluster's SFE. The possibility that gas is reaccreted by the cluster will affect the available gas reservoir for future star formation.

That we detect outflows only in three sources, or $\sim 8\%$ of the three dozen SSCs in the center of NGC 253 (Figure 1), gives credence to the idea that this outflowing phase must be short-lived. It is unlikely that we miss many sources with outflows due to their orientation and geometry because the modeling presented in Section 3.2 as well as simulations

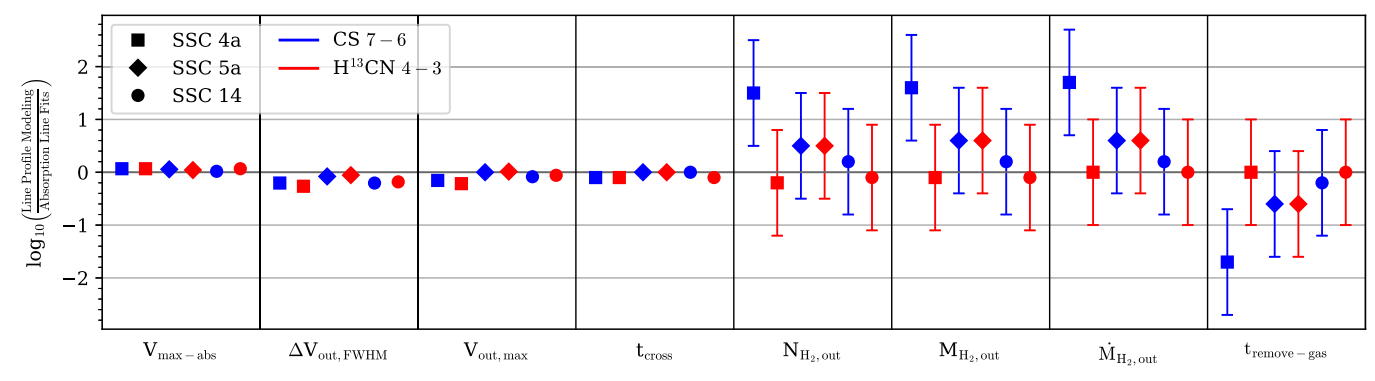


Figure 10. A comparison of common quantities measured from the absorption line fits (Section 3.1) and the line profile modeling (Section 3.2). Each bin (separated by black vertical lines) shows one quantity listed in Tables 2 and 3. Within the bins, points are artificially offset along the horizontal axis for clarity. The different symbols show the three SSCs and the colors show the quantities derived from the two spectral lines, as defined in the legend. The vertical axis shows the logarithm of the ratio of the quantities from each method, such that each major tick mark corresponds to an order of magnitude. The error bars for the first four quantities are negligible; the error bars on the last four quantities reflect the order-of-magnitude uncertainty on the abundance ratio of the molecule with respect to H_2 .

Table 4
A Comparison of Relevant Cluster Timescales and Ages

SSC Number	$\log_{10}(t_{\mathrm{ZAMS-age}})^{\mathrm{a}}$	$\log_{10}(t_{\rm ff})^{\rm b}$	$t_{ m ZAMS-age}/t_{ m ff}$	$\log_{10}(t_{\mathrm{cross}})^{\mathrm{c}}$	$\log_{10}(t_{\text{remove-gas}})^{\text{d}}$	$\log_{10}(t_{\rm dep})^{\rm e}$
4a	4.95	4.9	1.1	5.0	4.3 ± 0.7	6.6
5a	≳5	4.7	\gtrsim 2.0	4.6	5.5 ± 0.4	6.4
14	4.88	4.5	2.4	4.4	4.9 ± 0.4	6.8

Notes. For details, see the discussion in Section 4.1.

^a The age of the cluster since the ZAMS (t_{ZAMS-age}) calculated by the ratio of the luminosity in protostars to that in ZAMS stars from Rico-Villas et al. (2020).

(e.g., Geen et al. 2021) suggest that the outflows are wide. We could, however, be missing outflows if the outer layers of dense gas are very optically thick, which could obscure the outflows (e.g., Aalto et al. 2019) or if there are weak outflows below our sensitivity or cluster mass detection limits. Given that it is expected that the SSCs begin disrupting their natal clouds after $\sim 10^{5-6}$ yr (Johnson et al. 2015) and taking $t_{\rm cross} = 10^{4.5}$ yr as the lower limit on the age of the outflow, we would expect to find outflows in at least 3%–30% of SSCs, which agrees well with our detection rate of 8%. This percentile range is a lower limit because $t_{\rm cross}$ is the minimum possible age of the outflow and there could be additional outflows below our detection limit, though they would be weak. This also assumes that the clusters formed at the same time, which is also unlikely.

In general the chemistry-based age sequences presented by Krieger et al. (2020) lead to different relative cluster ages than the dynamical progression presented here, which are also different from the ZAMS age sequence of Rico-Villas et al. (2020). It is important to keep in mind, however, that the oldest clusters are not necessarily the most evolved, and vice versa. Using HCN/HC₃N as a relative age tracer, Krieger et al. (2020) suggested that SSCs 4 and 14 are in the younger

half of the SSCs studied, while SSC 5 is among the oldest. An age sequence using the chemistry of sulfur bearing molecules suggests instead that SSCs 5 and 14 are younger, whereas SSC 4 is older (Krieger et al. 2020). This is in disagreement with the age progression suggested by Rico-Villas et al. (2020), who suggested an inside out formation with SSCs 4 -12 being the oldest and SSCs 1-3, 13, and 14 being the youngest. The detections of outflows toward SSCs 4a, 5a, and 14 would suggest that they are the most evolved clusters in the young burst, in the simplest model where the clusters completely and finally clear their gas at the end of their formation periods. As described in the following section, SSC 5a may be among the most evolved clusters, as it is the only one of these clusters visible in the NIR. Krieger et al. (2020) also found the lowest dense gas ratios in SSC 5a, suggesting that it has expelled and/or heated and dissociated much of its natal molecular gas. Given the gas-rich environment surrounding these clusters, however, it is possible that other clusters are older and more evolved, but have reaccreted gas from the surrounding medium or that was not completely expelled. Given that the mean velocities of the outflows in SSCs 4a, 5a, and 14 are less than the escape velocities, this is perhaps a likely scenario.

^b The freefall time ($t_{\rm ff}$) calculated by Leroy et al. (2018). For SSC 4a, the value for SSC 4 is used because SSC 4a is the dominant component of the SSC 4 complex. The uncertainty introduced by this assumption is likely minor compared to other uncertainties, which are ~0.4–0.5 dex (see Table 2 of Leroy et al. 2018).

^c The time for gas to travel from the center of the cluster to the radius of the continuum source (r_{SSC}) at the typical outflow velocity $(V_{max-abs})$. This timescale (t_{cross}) is a proxy for the age of the outflow. For each SSC, this is the average of the values in Tables 2 and 3.

The time for the entire gas mass of the cluster (from Leroy et al. 2018) to be depleted at the current $\dot{M}_{\rm H_2,outflow}$. For each SSC, this is the average of the values in Tables 2 and 3. Uncertainties reported in the table are the standard deviations of the mean values from Table 2 and the values in Table 3. Propagated systematic uncertainties (due to the uncertainty in the molecular abundances) are 0.4 dex.

^e The gas depletion timescale, defined as $t_{\text{dep}} \equiv \frac{M_{H_2,\text{tot}}}{\text{SFR}_{36\,\text{GHz}}}$. For SSC 4a, the gas mass for SSC 4 is used because SSC 4a is the dominant component of the SSC 4 complex.

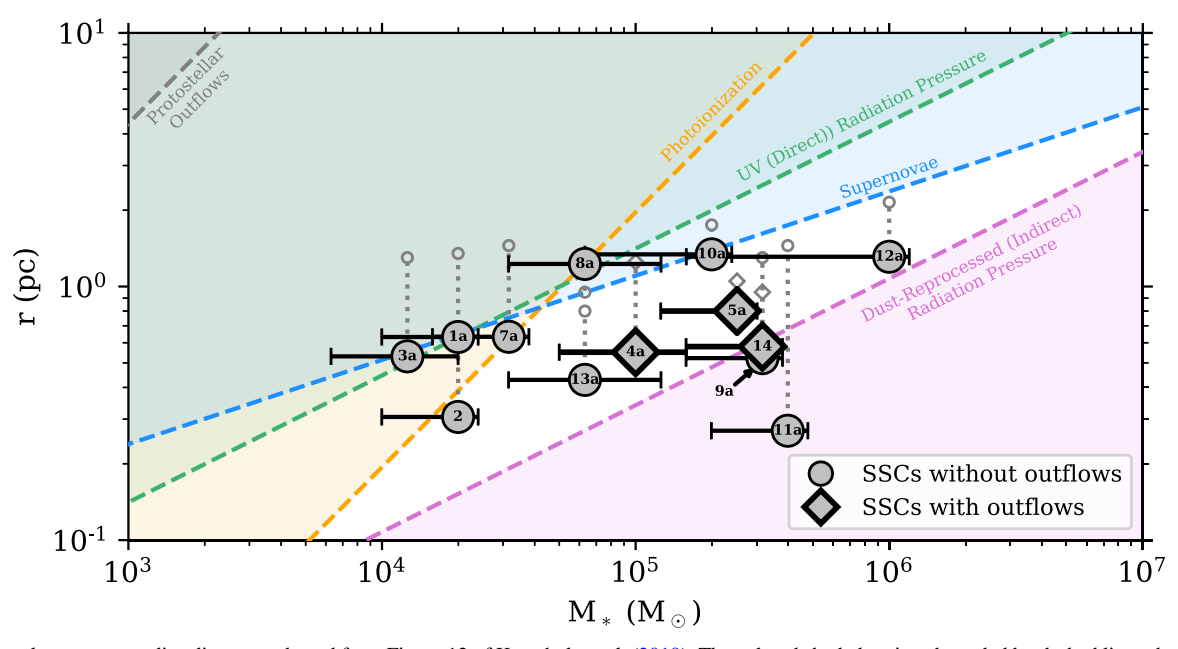


Figure 11. The cluster mass–radius diagram, adapted from Figure 12 of Krumholz et al. (2019). The colored shaded regions bounded by dashed lines show the regions of this parameter space where the corresponding feedback mechanism is efficient. There is a locus where none of these feedback mechanisms are expected to be efficient, resulting in high SFEs. The circles show the primary SSCs in NGC 253 without evidence for outflows, and the diamonds show those with outflows. The cluster stellar masses (M_*) are from Leroy et al. (2018). The error bars include differences with measurements from RRLs (E. A. C. Mills et al. 2021, in preparation), systematics due to assumptions about the Gaunt factor, and conservative estimates of the effects of the clusters resolving into multiple smaller clusters. Not shown are unquantified uncertainties related to absorption of ionizing photons by dust and evolution beyond the ZAMS, both of which would result in higher values of M_* than reported. See Section 2.6 for details on the calculation of the error bars. The radii are our measured 350 GHz half-flux radii (Table 1), which are smaller than the radii previously measured by Leroy et al. (2018) (gray open symbols in the same style as in the legend) due to the increase in the spatial resolution of these observations. The change in radius is shown by the vertical gray dotted lines connecting the symbols. Notably, the SSCs with outflows lie within or near the locus where feedback is expected to be inefficient.

4.2. Outflow Mechanics

There are a handful of feedback mechanisms relevant for setting the SFE of star clusters. These include proto-stellar outflows, supernovae, photoionization, UV (direct) radiation pressure, dust-reprocessed (indirect) radiation pressure, and stellar winds. Each of these processes is efficient in driving outflows for different cluster masses, radii, and ages. One way to visualize this is through a mass-radius diagram (e.g., Fall et al. 2010; Krumholz et al. 2019), as shown in Figure 11. There is a locus where none of the feedback mechanisms considered by Krumholz et al. (2019) are efficient, and so clusters with those masses and radii should grow with high SFEs. An important caveat of this figure is that there are other parameters relevant to whether a feedback mechanism is efficient, such as the momentum carried by each mechanism and the timescales over which it operates, which are not shown in this representation.

We show in Figure 11 the primary SSCs in NGC 253, where SSCs without outflows are shown as circles and those with outflows are shown as diamonds. The radii are our measured half-flux radii listed in Table 1. Because of the factor of 4 improvement in the linear spatial resolution with respect to the observations reported by Leroy et al. (2018), the radii of these clusters are smaller than reported by Leroy et al. (2018). As a result, the clusters are systematically shifted down in Figure 11 as shown by the vertical dotted gray lines. The stellar masses are taken from Leroy et al. (2018), as described in Section 2.6. We note, in particular, that the reported stellar masses may be underestimated (beyond the error bars) due to uncertainties about dust absorption and evolution beyond the ZAMS.

Many of the SSCs in NGC 253 fall inside the white area of inefficient feedback in Figure 11, which suggests that none of those mechanisms may be efficient for these clusters. The detection of outflows in SSCs 4a, 5a, and 14, however, means there is direct evidence of strong feedback. The H₂ masses in the outflows are significant compared to the total mass in the cluster itself (Table 2). From the previous section (and quantified in Table 4), the gas-removal times $(t_{\text{remove-gas}})$ based on the current mass outflow rates are much shorter than the timescale for future star formation ($t_{\rm dep}$). Comparison of these timescales implies that the outflows will remove the molecular gas faster than it would otherwise be used up by star formation. Note that these timescales assume either a constant mass outflow rate or a constant SFR, respectively, neither of which is likely to be the case in reality. Moreover, $t_{\text{remove-gas}}$ assumes there is no new infall replenishing the reservoir, and t_{dep} assumes no molecular gas is removed. Nevertheless, the outflows will have a non-negligible effect on the reservoir of gas available to the cluster to form stars and hence on the cluster's SFE.

What mechanism, then, is powering these outflows, given that SSCs 4a and 5a lie in the locus where no mechanism is expected to be efficient and SSC 14 is near a boundary? We explore four plausible mechanisms shown in Figure 11 below (excluding proto-stellar outflows that are only important for much lower-mass clusters; e.g., Guszejnov et al. 2021). We also consider winds from high-mass stars that may be important for clusters of these masses and ages (e.g., Gilbert & Graham 2007; Agertz et al. 2013; Geen et al. 2015; Lancaster et al. 2021a, 2021b). In addition to their location in the mass-radius diagram (a reframing of their surface densities),

we also compare the momentum expected to be carried by each of these processes and the timescales over which they operate to the values estimated for these clusters. It is also possible that a synergistic combination of mechanisms is at work (e.g., Rahner et al. 2017, 2019). These potential scenarios are discussed in the reminder of this section.

4.2.1. Supernovae

These clusters are young ($\sim 10^5$ yr; Rico-Villas et al. 2020), and so it is not expected that many, if any, supernovae have exploded since it typically takes ~3 Myr before the first supernova explosion (e.g., Zapartas et al. 2017). Moreover, the expected cloud lifetimes in a dense starburst like NGC 253 are expected to be shorter than 3 Myr (e.g., Murray et al. 2010), meaning that clouds would be disrupted before supernova feedback would be important. The gas-removal times estimated for these outflows are $\ll 3$ Myr in all cases (Table 4), supporting the idea that the clusters are too young for supernovae. Even with the large uncertainties, the radial momentum we measure in their outflows (Table 2) is an order of magnitude or more lower than expected for supernovadriven outflows (1000–3000 km s⁻¹; e.g., Kim & Ostriker 2015; Kim et al. 2017a). Finally, E. A. C. Mills et al. (2021, in preparation) constructed millimeter SEDs of these SSCs at 5 pc resolution and found that all three of these sources have negligible synchrotron components, further ruling out supernovae as the mechanism driving the cluster outflows.

4.2.2. Photoionization

Photoionization can remove a substantial amount of gas from a cluster, depending primarily on the density of the cluster (e.g., Kim et al. 2018; He et al. 2019; Dinnbier & Walch 2020; Geen et al. 2020, 2021). He et al. (2019) studied the effects of photoionization on massive star clusters, finding that photoionization is most efficient at suppressing star formation in lower density clusters. Similarly, Dinnbier & Walch (2020) found that photoionization (and winds) are inefficient at clearing the natal gas from clusters with masses $>5 \times$ $10^3 M_{\odot}$, unless they form with a high SFE. Though simulating different size and mass scales, Dinnbier & Walch (2020) and Geen et al. (2020, 2021) found that feedback by photoionization is most important at the outer layers of the cloud or HII region. Kim et al. (2018) found that the momentum carried by a photoionization-driven outflow decreases with increasing cluster surface density. Assuming that the dense gas we measure follows the trends for the neutral gas simulated by Kim et al. (2018) and that the trends continue to these higher surface densities, the radial momentum per unit mass from photoionization should be very small $(p_r/\bar{M}_* \lesssim 1 \text{ km s}^{-1})$ for the molecular gas surface densities of SSCs 4a, 5a, and 14 of $\Sigma_{\rm H_2} \sim 10^{4.2-4.9}~M_\odot~{\rm pc}^{-2}$ (Leroy et al. 2018). Using the stellar masses and radii, we can calculate the estimated ionized gas masses and momentum (using Equations 3, 4, and 11 of Leroy et al. 2018) and assuming $V_{\rm ion} = 15~\rm km~s^{-1}$ (as below), finding the $p_{\rm ion}/M_* \approx 0.13, 0.15$, and 0.08 km s⁻¹ for SSCs 4a, 5a, and 14. We note that the ionizing photon rates estimated by Leroy et al. (2018) for these sources are consistent with a new analysis by E. A. C. Mills et al. (2021, in preparation). These estimated momenta based on the ionizing photons are much smaller than the measured values of $p_r/M_* \approx 5-126$, 1-3, and 5–40 km s $^{-1}$ (Table 2).

Krumholz et al. (2019) parameterized the effect of photoionization in terms of the ionized gas sound speed ($c_{s,\rm ion}$) and the cluster escape velocity ($V_{\rm esc}$), such that photoionization will be efficient when $c_{s,\rm ion} > V_{\rm esc}$. It is thought that the photoionization will be efficient for clusters with $V_{\rm esc} \approx c_{s,\rm ion} \leq 10\,\rm km\,s^{-1}$. Figure 11 and Krumholz et al. (2019) assume $V_{\rm esc} \approx c_{s,\rm ion} = 15\,\rm km\,s^{-1}$. The escape velocities of SSCs 4a, 5a, and 14 are approximately 23, 34, and 50 km s⁻¹, respectively. This suggests photoionization could be important for SSC 4a, but the escape velocities of SSCs 5a and 14 are likely too large for this mechanism to be efficient. This is in agreement with the qualitative results of simulations discussed above.

Therefore, feedback from photoionization likely plays a minor role in driving these outflows as these clusters are dense and hence their escape velocities are too large for photoionization to efficiently drive outflows.

4.2.3. UV (Direct) Radiation Pressure

There are many studies that investigate the role of UV (direct) radiation pressure in driving outflows and expelling gas from a molecular cloud or HII region (e.g., Kim et al. 2016, 2017b, 2018, 2019; Raskutti et al. 2017; Crocker et al. 2018a, 2018b; Barnes et al. 2020; Dinnbier & Walch 2020). In general, many of these studies have found that UV radiation pressure can play an important—if not dominant—role in expelling gas from a cluster, especially for low surface density clouds (e.g., Skinner & Ostriker 2015; Raskutti et al. 2017). Using a numerical radiation hydrodynamic approach, Raskutti et al. (2017) studied the effects of radiation pressure from nonionizing UV photons on massive star-forming clouds, finding that over a cloud's lifetime \$\geq 50\% of the UV photons escape through low-opacity channels induced by turbulence and hence do not contribute to radiation pressure-driven outflows. An important caveat is that the clouds simulated by Raskutti et al. (2017) are larger in size and so have lower densities than the clusters in NGC 253. Raskutti et al. (2017) found that the mean outflow velocity of their radiation pressure-driven outflows is \sim 1.5-2.5 $V_{\rm esc}$, independent of cloud surface density. For the clusters in NGC 253, this translates to expected mean outflow velocities of \sim 33–114 km s⁻¹, faster than the observed mean velocities of 6–28 km s⁻¹. The radial momentum per unit stellar mass (p_r/M_*) of SSCs 4a, 5a, and 14 are an order of magnitude or more less than measured by Raskutti et al. (2017) for clouds of roughly the same initial mass, though the clusters in NGC 253 are denser than the simulated clouds. In contrast, the clusters in NGC 253 have slightly larger radial momenta per unit of outflowing mass (p_r/M_{out}) . This means that the clusters in NGC 253 have less outflowing mass relative to their stellar masses than the simulated clusters, though this could also be due to the difference in cloud densities.

Simulations of feedback from photoionization and UV radiation pressure by Kim et al. (2018) found $t_{\rm dep} \sim 2.5$ Myr for their densest clouds ($\Sigma_{\rm neutral} = 10^3~M_\odot~{\rm pc}^{-2}$). Our clusters, which have $\Sigma_{\rm H_2} \sim 10^{4.4-5.3}~M_\odot~{\rm pc}^{-2}$ (Leroy et al. 2018), have $t_{\rm dep} = 2.5-6.3$ Myr, whereas extrapolation of the Kim et al. (2018) calculations would result in lower values of $t_{\rm dep}$ if the trends continue to these higher densities. Kim et al. (2018) also found a relatively constant outflow velocity of $\sim 8~{\rm km~s}^{-1}$, approximately independent of surface density in the neutral phase. This is similar to the mean outflow velocities of the dense gas traced by CS 7–6 or H¹³CN 4–3 for SSC 4a ($\approx 7~{\rm km~s}^{-1}$), but lower than those for SSCs 5a and 14 (≈ 22

and 25 km s⁻¹, respectively). In terms of momentum, according to Equation (18) in Kim et al. (2018), an outflow driven by photoionization and UV radiation pressure would have a momentum per unit stellar mass of \sim 1 km s⁻¹ at the surface densities observed in our clusters. This is about an order of magnitude lower than the p_r/M_* measured for dense gas traced by CS 7–6 or H¹³CN 4–3 in these clusters (though our uncertainties are large). An important caveat to this is that the clusters in NGC 253 are denser than those simulated by Kim et al. (2018). Additionally, these simulations probe the neutral outflowing phase, whereas our observations probe the outflowing dense molecular gas.

The efficiency of UV radiation pressure can be parameterized in terms of the surface mass density of the cluster (Σ) compared to the the outward force of radiation pressure. Skinner & Ostriker (2015) and Krumholz et al. (2019) defined a critical surface density, $\Sigma_{\rm DR} = \frac{\Psi}{4\pi Gc}$, where Ψ is the light-to-mass ratio, below which UV radiation pressure becomes important. A population of ZAMS stars that fully samples a Chabrier (2003) initial mass function (IMF) has $\Psi \approx 1100 L_{\odot}$ M_{\odot}^{-1} (e.g., Fall et al. 2010; Kim et al. 2016; Crocker et al. 2018a), resulting in $\Sigma_{\rm DR} \approx 340~M_{\odot}~{\rm pc}^{-2}$. Models and simulations show that UV radiation is only effective for surface densities $\Sigma \lesssim 10~\Sigma_{DR}$ because turbulence will introduce low-column sight-lines that allow the radiation to escape (e.g., Thompson & Krumholz 2016; Grudić et al. 2018; Krumholz et al. 2019). The value of Σ_{DR} depends principally and linearly on the assumed light-to-mass ratio and hence on the IMF. SSCs 4a, 5a, and 14 are all well below this boundary shown in green in Figure 11, meaning that a significantly top-heavy IMF resulting in a much higher value of Ψ is required for these outflows to be powered solely by UV radiation pressure. A topheavy IMF has been suggested in other massive or SSCs (e.g., Turner et al. 2017; Schneider et al. 2018). Turner et al. (2017) found a top-heavy IMF in an SSC in NGC 5253 with $\Psi \approx 2000~L_{\odot}M_{\odot}^{-1}$. However, an unphysically large light-tomass ratio $\sim 10,000 \, L_{\odot} \, M_{\odot}^{-1}$ is needed for UV radiation to explain the feedback in SSCs 4a, 5a, and 14.

It is, therefore, unlikely that UV (direct) radiation pressure is the dominant mechanism responsible for driving the outflows in SSCs 4a, 5a, and 14.

4.2.4. Dust-reprocessed (Indirect) Radiation Pressure

Given the large dust columns in these SSCs, dust-reprocessed (indirect) radiation pressure is a promising mechanism to power the outflows. In a study of massive star clusters in the Milky Way's Central Molecular Zone, Barnes et al. (2020) found that indirect radiation pressure is important at early times (<1 Myr). Similarly, Olivier et al. (2021) found that dust-reprocessed radiation pressure is the dominant feedback mechanism in ultra-compact H II regions in the Milky Way. Moreover, given the possible underestimate of the stellar masses due to absorption of ionizing photons by dust or evolution beyond the ZAMS (which are not reflected in the error bars in Figure 11), indirect radiation pressure is a plausible mechanism to drive the observed outflows.

Whether the dust-reprocessed radiation pressure can drive an outflow fundamentally depends on the balance between the outward force of the radiation pressure and the inward force of gravity (i.e., the Eddington ratio, $f_{\rm Edd}$). This depends on the dust opacity and the input luminosity from the cluster, which can be parameterized by the light-to-mass ratio of the assumed

IMF. The dust opacity (κ_d) quantifies a dust grain's ability to absorb IR radiation. As explored by Semenov et al. (2003), this quantity varies with temperature, dust composition, grain shape, grain size distribution, and the opacity model. For example, grains in dense molecular clouds exhibit larger κ_d than those in the diffuse ISM, which is thought to be due to the growth of mantles (e.g., Ossenkopf & Henning 1994). Given the high-density and intense radiation environment in these clusters, the dust opacity may be quite different than found in Galactic regions, though we have no precise observational constraints on how much κ_d can vary in these environments. Oftentimes, a dust-to-gas ratio (DGR) is assumed to convert the dust opacity to the opacity in the gas, and the standard Solar Neighborhood value is DGR = 0.01. Finally, the light-to-mass ratio (Ψ) depends on the assumed IMF, where a top-heavy IMF will have a larger value of Ψ . Top-heavy IMFs have been claimed in massive clusters with $\Psi \sim 2000\,L_\odot\,M_\odot^{-1}$ (e.g., Turner et al. 2017; Schneider et al. 2018) compared to either a Kroupa (2001) or Chabrier (2003) IMF, which have $\Psi = 883 L_{\odot} M_{\odot}^{-1}$ and $\Psi = 1100 L_{\odot} M_{\odot}^{-1}$, respectively. Models have also found that the IMFs of globular cluster progenitors—thought to be SSCs—are more top heavy with increasing density and decreasing metallicity (Marks et al. 2012). For clusters with the stellar masses and densities of those in NGC 253 (Leroy et al. 2018), we would expect a typical high-mass IMF slope. Toward constraining the nature of the IMF in these clusters, E. A. C. Mills et al. (2021, in preparation) measured the fraction of ionized helium toward these SSCs using H and He RRLs at 5 pc resolution. This ratio is expected to be somewhat dependent on the IMF, as a topheavy IMF will result in more massive stars capable of ionizing He. E. A. C. Mills et al. (2021, in preparation) measured massweighted He⁺ fractions that are consistent with He⁺ fractions found in HII regions in the center of the Milky Way (e.g., Mezger & Smith 1976; de Pree et al. 1996; Lang et al. 1997), which is not thought to have a globally top-heavy IMF (e.g., Löckmann et al. 2010), though there are individual clusters that do seem to favor a top-heavy IMF (e.g., Lu et al. 2013). While the measured He⁺ fractions do not completely rule out the possibility of a top-heavy IMF (it is unclear precisely how much the He⁺ fraction changes with the IMF), it is unlikely that the IMF in these clusters is extremely top heavy.

Below we describe two approaches taken by simulations in determining the efficiency of dust-reprocessed radiation pressure in driving outflows, and discuss how adjustments to the fiducial assumptions on κ_d , DGR, and Ψ may help explain the outflows observed in SSCs 4a, 5a, and 14.

Numerical simulations of dust-reprocessed radiation pressure by Skinner & Ostriker (2015) assumed that the dust opacity (κ_d) is constant with temperature (and hence distance from the UV source). Skinner & Ostriker (2015) found

$$f_{\rm Edd} = 0.68 \left(\frac{\rm DGR}{0.01}\right) \left(\frac{\kappa_d}{0.1 \, \rm cm^2 \, g^{-1}}\right) \left(\frac{\Psi}{883 \, L_{\odot} \, M_{\odot}^{-1}}\right), \tag{4}$$

where we have explicitly included the dependence on the DGR. For the fiducial values of the DGR and Ψ , Skinner & Ostriker (2015) found $f_{\rm Edd} > 1$ only for $\kappa_d > 0.15~{\rm cm}^2~{\rm g}^{-1}$, which is unphysically large for Solar Neighborhood–like dust properties (typically $0.03~{\rm cm}^2~{\rm g}^{-1}$; Semenov et al. 2003). If, however, the dust is different in these environments than in the Solar

Neighborhood, κ_d could be larger, though we have no observational constraints to evaluate this. Assuming Solar Neighborhood-like dust and a Kroupa (2001) IMF, we can achieve $f_{Edd} > 1$ if the DGR is > 0.05. Although the center of NGC 253 is known to have a super-solar metallicity (Z = 2.2 Z_{\odot} ; Davis et al. 2013) and the clusters may be even more dust rich (Turner et al. 2015; Consiglio et al. 2016), a DGR > 0.05seems quite high. Turning instead to the possibility of a topheavy IMF, Equation (4) yields $f_{\rm Edd} > 1$ for $\Psi > 4300 L_{\odot} M_{\odot}^{-1}$ (for Solar Neighborhood–like values of κ_d and DGR,), which is much more top heavy than has been found in other SSCs (e.g., Turner et al. 2017). Given that E. A. C. Mills et al. (2021, in preparation) did not find strong evidence for an increased He⁺ fraction in these clusters, a very top-heavy IMF is unlikely. Finally, Skinner & Ostriker (2015) noted that for clustered sources of UV photons—almost certainly the case in the SSCs in NGC 253—there can be appreciable cancellation of the radiation pressure terms from each source, so that the net momentum to drive a cluster-scale outflow will be lower, independent of increases in the DGR, κ_d , or Ψ . Therefore, while there may be some combination of increased κ_d , DGR, and Ψ that enables dust-reprocessed radiation pressure to efficiently drive outflows in these clusters, it is unclear how much internal cancellation will affect the net momentum.

Crocker et al. (2018a) took a slightly different approach to study the efficiency of dust-reprocessed radiation pressure. Modeling of the Rosseland mean opacity by Semenov et al. (2003) found $\kappa_d \propto T^2$ for $T < 100\,\mathrm{K}$. Crocker et al. (2018a) converted this temperature dependence into a radial dependence from the central source of UV photons, introducing a gradient in κ_d . This has the effect of boosting the effective dust opacity for clusters that are very dense, allowing for outflows to be driven more easily compared to Skinner & Ostriker (2015). Second, this allows Crocker et al. (2018a) to express their $f_{\rm Edd}$ in terms of a critical surface density:

$$\Sigma_{*,IR} = (1.3 \times 10^{5} M_{\odot} \text{ pc}^{-2}) \times \left(\frac{\kappa_d}{0.03 \text{ cm}^2 \text{ g}^{-1}}\right)^{-1} \left(\frac{\Psi}{1100 L_{\odot} M_{\odot}^{-1}}\right)^{-1} \left(\frac{\text{DGR}}{0.01}\right)^{-1},$$
 (5)

where we have again explicitly shown the dependence on the DGR. The pink dashed boundary in Figure 11 assumes the fiducial values of κ_d , Ψ , and DGR. While SSC 14 lies on this boundary, SSCs 4a and 5a fall above it, suggesting that dust-reprocessed radiation pressure is not sufficient for driving outflows in these clusters.

Note, however, that there are considerable uncertainties in this picture. The cluster stellar masses may be underestimated if appreciable ionizing photons are absorbed by dust or if the stellar population is evolved beyond the ZAMS. Therefore, they may be closer to the region where dust-reprocessed radiation pressure is more efficient than shown in Figure 11. Moreover, we do not fully understand the properties of dust in these conditions. As discussed above, the DGR in their surrounding gas may be $\gtrsim 0.022$ given the observed supersolar metallicity in the center of NGC 253 (Davis et al. 2013) and the high-density conditions in the starburst molecular gas, which may favor dust formation. Assuming DGR = 0.022 in Equation (5), moves the $\Sigma_{*,\rm IR}$ boundary up to encompass SSCs 4a and 5a. This difference compared to the results of

Skinner & Ostriker (2015) comes from the assumed temperature dependence in κ_d , which provides a boosted dust opacity for very compact sources. This itself is very uncertain, since the dust models are designed for proto-planetary disks, and the growth of κ_d with T saturates at $T \sim 100$ K (see Semenov et al. 2003). Considering changes to the IMF using the fiducial value of κ_d and the DGR would require $\Psi \gtrsim 3000 L_{\odot} M_{\odot}^{-1}$ to explain SSCs 4a and 5a, or $1.5 \times$ more top heavy than the IMF in NGC 5253 (Turner et al. 2017). Even with the boost in κ_d , there would still be cancellations in the radiation pressure due to clustered UV sources, although these cancellations may not be as severe as in the constant κ_d case.

Therefore, it is possible that dust-reprocessed (indirect) radiation pressure could drive the outflows observed in SSCs 4a, 5a, and 14, though this hinges critically on the behavior of the dust opacity (κ_d) for which there are no observational constraints in these extreme environments. A likely elevated DGR in these sources helps, but cancellations from clustered UV sources hinders the efficiency with which dust-reprocessed radiation pressure can drive outflows. Therefore, whether dust-reprocessed radiation plays a dominant role in powering the outflows observed from SSCs 4a, 5a, and 14 is an open question.

4.2.5. Winds from High-mass Stars

Given the stellar masses of these clusters ($M_* = 10^{5.0-5.5} M_{\odot}$), we would expect $\gtrsim 1000-3000$ O stars in each cluster, assuming a Kroupa (2001) IMF. It has been suggested that outflows from young, massive SSCs in the Antennae are driven by a combination of O and Wolf–Rayet (WR) stellar winds (Gilbert & Graham 2007), although other possible mechanisms are not evaluated. The combined power of the winds from these massive stars could, therefore, play an important role in powering the outflows from the clusters in NGC 253.

It has been suggested that winds from WR stars significantly impact how a cluster clears its natal gas, as they impart $\sim 10 \times$ the energy of O-star winds over a shorter period of time (e.g., Sokal et al. 2016). The mass-loss rates of WR stars are metallicity dependent, with higher mass-loss rates at higher metallicity for both carbon- and nitrogen-rich WR stars (Vink & de Koter 2005). Because WR stars are evolved O stars, it is thought that they should not contribute much toward the cluster feedback until after \sim 3–4 Myr, when other processes such as supernovae are becoming important and when much of the natal gas has already been dispersed. In an observational study of massive embedded clusters, however, Sokal et al. (2016) found that WR winds are important even at earlier stages, though the clusters they studied all have ages >1 Myr. Moreover, they found that clusters without WR stars tend to stay embedded longer than those with WR stars, indicating that WR winds may accelerate the gas-clearing stage.

It is unclear, however, whether the clusters in NGC 253 harbor WR stars yet, given their very young ages ($t_{\rm ZAMS-age} \approx 0.1$ Myr). There is evidence of a WR population toward SSC 5—perhaps the most evolved cluster—but higher spatial and spectral resolution observations are needed to confirm this (Kornei & McCrady 2009; Davidge 2016). There is a known WR X-ray binary in NGC 253, but it is outside of the nuclear region studied here by \sim 250 pc in projection (Maccarone et al. 2014). Given the young ages of these clusters, it is unlikely that there are many, if any, WR stars present in these clusters, especially SSCs 4a and 14. Once a

portion of the O star population evolves into WR stars, however, their winds could potentially strongly contribute to driving outflows.

Simulations of stellar wind feedback on the clearing of a cluster's natal gas have mixed conclusions. Some simulations show that stellar winds are important at early times in a cluster's life, especially for clearing the natal dense gas before supernovae start occurring at around 3 Myr (e.g., Agertz et al. 2013; Geen et al. 2015, 2020, 2021). Given that the clusters in NGC 253 are substantially younger than this ($t_{\rm ZAMS-age} \approx 0.1$ Myr), stellar winds may play a prominent role in driving the outflows we observe from these SSCs. Other simulations, however, have found that stellar winds are most effective after 3 Myr (Calura et al. 2015). There are also simulations that have found that stellar winds (and photoionization) alone cannot expel the natal gas for massive ($>5 \times 10^3 M_{\odot}$) clusters at any time point unless they form with an SFE $\equiv M_*/(M_{\rm gas} + M_*) > 1/3$ (Dinnbier & Walch 2020).

In the absence of gas cooling, stellar winds can impart momentum into the surrounding material typically $p_r/M_*\approx 50$ –65 km s⁻¹ (Weaver et al. 1977), assuming a wind luminosity of 10^{34} erg s⁻¹ (Starburst99; Leitherer et al. 1999), the ages of these clusters to be $\approx 10^5$ yr (Rico-Villas et al. 2020) and $n_{\rm H}=10^5$ cm⁻³. These estimates are on the high side of our observed range of $p_r/M_*\approx 5$ –126, 1–3, and 5–40 km s⁻¹ for SSCs 4a, 5a, and 14, respectively (Table 2), and are fairly insensitive to the assumed average gas density (an order of magnitude in $n_{\rm H}$ results in a factor of ≈ 1.5 change in the expected momentum).

If the gas can cool, however, the momentum imparted will be substantially lower, and this is especially relevant in the large ambient densities found near these SSCs (e.g., Silich et al. 2004; Palouš et al. 2014; Lochhaas & Thompson 2017; Wünsch et al. 2017; El-Badry et al. 2019; Gray et al. 2019; Lancaster et al. 2021a, 2021b). An outflow stalled by cooling has been claimed in a SSC in NGC 5253 (Cohen et al. 2018). Nonetheless, recent simulations by Lancaster et al. (2021a, 2021b) found that although cooling is important for the gas densities in the central starburst of NGC 253, the momentum imparted with significant cooling still provides a modest enhancement over a momentumconserving wind. The computed enhancement factor (α_p) is sufficient to power outflows even with efficient cooling (with $\alpha_p \approx 1$ –4 assuming a normal IMF and solar metallicity). For the typical ages of these SSCs (~0.1 Myr), Lancaster et al. (2021a, 2021b) predicted a momentum injection of $p_r/M_* \approx$ $0.8\,\mathrm{km\,s^{-1}}$, lower than momenta measured for SSCs 4a, 5a, and 14 of $p_r/M_* \approx 5-126$, 1-3, and 5-40 km s⁻¹ (Table 2). Given the predicted shell velocity from Lancaster et al. (2021a, 2021b), we can estimate the value of α_p implied by the observed outflows:

$$\alpha_p = \left(\frac{V_{\text{max-abs}}}{2.0 \text{ km s}^{-1}}\right)^2 \left(\frac{M_{\text{H}_2}, \text{ out}}{M_{*}}\right) \left(\frac{r_{\text{SSC}}}{1 \text{ pc}}\right)^{-1}.$$
 (6)

For the measured outflow properties of SSCs 4a, 5a, and 14, this suggests $\alpha_p \approx 9$ –227, 4–10, and 34–272, respectively (using the parameters in Tables 1 and 2) compared to $\alpha_p \approx 1$ –4 from the simulations. For all SSCs, our values of M_* may be underestimated (Section 2.6), reducing the values of α_p inferred from Equation (6). A top-heavy IMF could provide up to a factor of 4 enhancement in the strength of the wind (Lancaster et al. 2021a, 2021b). As described in Section 4.2.4, we do not expect the IMF in these clusters to

be particularly top heavy (e.g., Marks et al. 2012, E. A. C. Mills et al. 2021, in preparation), although this possibility cannot be ruled out entirely. The wind strength can also be enhanced if the metallicity is super solar, as is likely the case for these clusters (Davis et al. 2013; Turner et al. 2015; Consiglio et al. 2016).

Given the uncertainties in our measured masses, the IMF, and the metallicity, it is possible that the outflow in SSC 5a is powered by stellar winds. Given the concerns about saturation in SSC 4a, the outflowing mass may be overestimated and so our inferred α_p from Equation (6) may also be overestimated, meaning that the outflow from SSC 4a may also be driven (at least in part) by stellar winds. The outflow from SSC 14, on the other hand, is unlikely to be solely by stellar winds.

Therefore, O star winds are unlikely to be driving the outflow observed toward SSC 14 in NGC 253, although it is possible they play a role in driving the current outflows in SSCs 4a and 5a, especially if the current stellar masses of these clusters are underestimated and if the metallicities are super solar. The O star populations in these clusters are likely too young to host many WR stars, except perhaps in the case of SSC 5a, so the effect of WR star winds is likely negligible at this stage in the SSCs evolution.

4.2.6. Summary: What Mechanisms Power the Outflows?

To summarize the above exploration of possible feedback mechanisms, we find that the outflows from SSCs 4a, 5a, and 14 are difficult to explain, though they are likely powered by a combination of dust-reprocessed radiation pressure and stellar winds. All three clusters are too young for supernovae to have exploded and too dense for photoionization or UV (direct) radiation pressure to be efficient. Whether dust-reprocessed radiation pressure is efficient depends on the properties of the dust opacity (κ_d) , for which there are virtually no constraints in extreme environments like these SSCs, and likely requires some combination of a higher dust opacity, an increased dustto-gas-ratio, and a top-heavy IMF, all of which are currently poorly constrained in these clusters. Moreover, clustered UV sources within the SSCs can have the effect of canceling out the radiation pressure terms from other sources (Skinner & Ostriker 2015), reducing the net momentum to drive a clusterscale outflow. In the case of stellar winds, cooling is expected to be important for these clusters. Although recent simulations have found that even in the presence of strong cooling, O star stellar winds may be sufficient to power outflows (Lancaster et al. 2021a, 2021b), we find that the expected momentum is insufficient to explain the observed properties of the outflows in SSC 14 and possibly in SSC 4a. For SSC 14, the outflows are likely dominated by dust-reprocessed radiation pressure, whereas the outflow in SSC 5a may be dominated by stellar winds. For SSC 4a, the deep absorption renders the outflowing mass estimate especially uncertain and likely overestimated, so we can only say that the outflow in that cluster is likely a combination of dust-reprocessed radiation pressure and stellar winds. Therefore, the precise mechanism(s) powering these outflows remains uncertain.

4.3. SSC 5a and Hubble Space Telescope (HST) NIR Clusters

Several clusters and one SSC have been previously identified in the center of NGC 253 based on HST NIR images (Watson et al. 1996; Kornei & McCrady 2009), with the NIR-detected

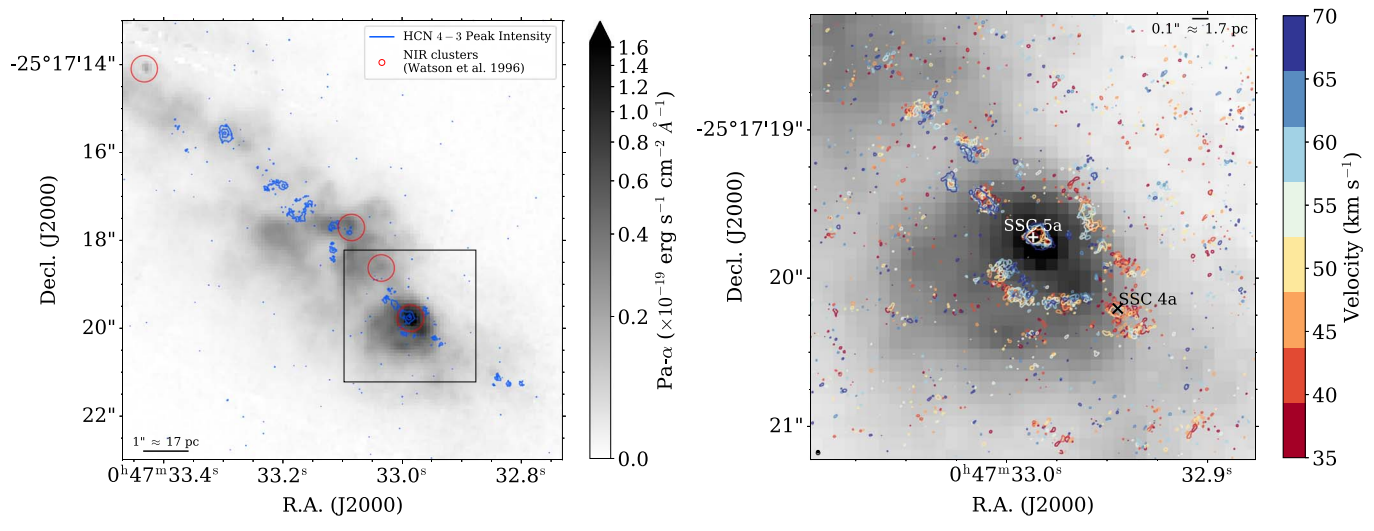


Figure 12. (Left) the HST $Pa-\alpha$ image. The blue contours show the ALMA HCN 4-3 peak intensity at 2, 5, and $10\times$ the rms of the peak intensity image. The red circles show the NIR clusters identified by Watson et al. (1996), where the size of the circle reflects their 0.3'' positional uncertainty. Only one of the primary clusters (SSC 5a) corresponds to the previously identified NIR clusters. (Right) the HST $Pa-\alpha$ image centered on SSC 5a (white plus sign) over the $3''\times3''$ black square from the left panel. There is an asymmetry in the $Pa-\alpha$ emission, which Kornei & McCrady (2009) posited may be due to an outflow. The contours show the HCN 4-3 emission in selected the velocity channels relative to the systemic velocity of SSC 5a (Table 2), showing a shell-like structure with a velocity gradient across the shell. The contours are drawn at $3\times$ the rms of the HCN 4-3 cube. The location of SSC 4a is also marked for context (black cross). The asymmetry in the $Pa-\alpha$ emission does not align with the HCN 4-3 shell. This shell of HCN 4-3 may be the signature of an earlier (stronger) outflow phase from SSC 5a.

SSC corresponding to SSC 5 (Leroy et al. 2018). To be able to see the NIR emission, the cluster must have dispersed much of its natal gas and dust or it aligns with a serendipitous hole in the extinction screen. If the presence of NIR emission at this cluster location is from gas clearing, this implies that the cluster must be older than the other, highly extincted clusters. As shown in Figure 6, we see evidence for a weak outflow in the dense gas tracers from this cluster, which may be the tail end of this gas dispersal process from the timescale arguments in Section 4.1. The measured mass outflow rate and momentum injection are also lower than for SSCs 4a and 14. It is important to note, however, that SSC 5a still has a high overall gas fraction $(M_{\rm H_2,tot}/M_*)$ of 0.8, though it is not as high as SSCs 4a and 14 (1.3 and 1.6, respectively).

Further support for this picture comes from the discovery of a shell near SSC 5a in HCN 4–3 as shown in Figure 12. This feature is too faint to be seen in CS 7–6 or $\mathrm{H}^{13}\mathrm{CN}$ 4–3 at this resolution. The shell is visible from \sim 35–70 km s⁻¹ relative to the cluster systemic velocity (Table 1) and has a projected radius of \sim 6 pc, though it is not perfectly centered on SSC 5a. Using these projected velocities, this implies an age of \sim 8–16 \times 10⁴ years. At its largest extent, the shell reaches the location of SSC 4a (in projection), which also has a dense gas outflow. This shell-like structure is not seen around any other SSCs.

Kornei & McCrady (2009) noted that the Pa- α emission around SSC 5a is asymmetric (Figure 12) and could be indicative of an outflow. We investigate how this asymmetric geometry corresponds to the observed shell in HCN 4–3. There are systematic offsets between the location of SSC 5a in the ALMA data, the NIR clusters identified in the HST Near Infrared Camera and Multi-Object Spectrometer (NICMOS) data by Watson et al. (1996) and the F187N and F190N HST NICMOS data used by Kornei & McCrady (2009). Leroy et al. (2018) corrected the positions of the Watson et al. (1996) NIR clusters by $\Delta\alpha$, $\Delta\delta=+0.32''$, -0.5'', so that the NIR cluster corresponding to SSC 5a has α , $\delta=00^{\rm h}47^{\rm m}32.985^{\rm s}$, $-25^{\circ}17^{\rm m}19.7^{\rm s}$ (J2000). The positions of the F187N and

F190N mosaics¹⁸ were corrected by matching the locations of the NIR clusters identified by Watson et al. (1996). A linear shift of $\Delta\alpha,\,\Delta\delta=+1.48'',\,-0.85''$ brings the HST images into agreement with the NIR clusters and the ALMA data sets. Figure 12 shows the Pa- α (F187N-F190N) image around SSC 5a with the HCN 4–3 contours overlaid. The expanding HCN 4–3 shell is not particularly aligned with the asymmetry seen in the Pa- α emission, though it does seem to align with the north-western edge.

It is therefore possible that this shell is a previous (stronger) version of the outflow detected spectrally in this work. The shell age of $\sim 10^5$ yr is in good agreement with the minimum ZAMS age and the end of the period of active gas accretion (Section 4.1). It is unlikely that the outflow is due to a supernova explosion both because synchrotron emission is a negligible component of SSC 5's SED (E. A. C. Mills et al. 2021, in preparation) and because the current momentum injection is well below what is expected from supernovae (e.g., Kim & Ostriker 2015; Kim et al. 2017a).

5. Summary

The central starburst in NGC 253 harbors over a dozen massive ($M_* \sim 10^5~M_\odot$, a likely lower limit inferred from RRLs and radio continuum) and extremely young star clusters, which are still very rich in gas and likely in the process of formation (Leroy et al. 2018, E. A. C. Mills et al. 2021, in preparation). Using high-resolution ($\theta \approx 0.028''$, equivalent to 0.48 pc) data from ALMA we study the 350 GHz (0.85 mm) spectra of these objects. We summarize our main results below, indicating the relevant figures and/or tables.

 $[\]overline{^{18}}$ These calibrated and reduced HST NICMOS (NIC2) images were downloaded from the Mikulski Archive for Space Telescopes (MAST) database from M. Rieke's 1998 August program with exposure times of $\approx\!384~\text{s}$. The mosaic tiles were stitched together using the <code>reproject</code> package in Astropy.

- 1. We observe P-Cygni line profiles—indicative of outflowing gas—in three SSCs in the center of NGC 253, sources 4a, 5a, and 14 (see Table 1). These line profiles can be seen in the full band spectra in many lines (Figure 3), and particularly cleanly in the CS 7–6 and H¹³CN 4–3 lines that are the focus of this analysis (Figures 1 and 6). Among these clusters, SSC 5a is notable for being the only one of the massive clusters that is observable in the NIR (Figure 12), suggesting it has cleared much of its surrounding gas.
- 2. By fitting the absorption line profiles (Figure 6), we measure outflow velocities, column densities, masses, and mass outflow rates (Table 2). The outflow crossing times—a lower limit on the outflow age—are short (\sim few \times 10⁴ yr), suggesting we are witnessing a short-lived phase. The outflowing mass in these objects is a non-negligible fraction of the total gas or stellar mass.
- 3. To place limits on the opening angles and line-of-sight orientations of the outflows, we construct a simple radiative transfer model aiming at reproducing the observed P-Cygni profiles in CS 7-6 and H¹³CN 4-3 (Figures 7 and 8). By varying the input temperatures, densities, velocities, and velocity dispersion of each component as well as the opening angle and orientation of the outflow component, we find that very wide opening angle models best reproduce the observed P-Cygni profiles (Figure 6). While we cannot precisely determine the opening angle for each cluster, the outflows must be almost spherical, although somewhat smaller opening angles are acceptable if the outflows are pointed almost perfectly along the line of sight (Figure 9). This modeling also provides measurements of the outflow velocity, column density, masses, and mass outflow rates (Table 3). In general, these two sets of measurements agree, given the large uncertainties (Figure 10).
- 4. We compare measurements of the ZAMS age (Rico-Villas et al. 2020) to the gas freefall time (Leroy et al. 2018), outflow crossing time, gas-removal time implied by the mass outflow rate, and the gas depletion time (Table 4). These estimates are consistent with the SSCs still being in a period of active gas collapse, though SSC 5a could be past this phase. The gas-removal timescale (assuming a constant mass outflow rate) is about an order of magnitude smaller than the gas depletion time due to star formation, showing that the outflows will have a substantial effect on the SFE of these SSCs. Reaccretion of gas that was expelled by the outflows is perhaps a likely scenario, which complicates the interpretation of the clusters' evolutionary sequences.
- 5. Given our measured velocities, masses, radii, surface densities, and momentum per unit stellar mass, we investigate the mechanisms responsible for driving the observed outflows. Possibilities are supernovae, photoionization, UV (direct) radiation pressure, dust-reprocessed (indirect) radiation pressure, and O star stellar winds. While none of these mechanisms completely explains the observations, the two explanations that are potentially in play are dust-reprocessed radiation pressure and stellar winds. It is possible that the outflows are powered by a combination of both mechanisms, with the feedback in SSC 14 dominated by dust-reprocessed

- radiation pressure and the feedback in SSC 5a dominated by stellar winds (Figure 11, Section 4.2).
- 6. We report the discovery of an expanding shell (seen in HCN 4-3) around SSC 5a with $r \sim 6$ pc (Figure 12). As mentioned above, SSC 5a is the only cluster visible in the NIR, which coupled with it having only a lower limits on the ZAMS age suggests that SSC 5a is the most evolved cluster. SSC 5a also has the weakest P-Cygni profile among the three detected and the smallest current mass outflow rate. Given its velocity and size, the shell is $\sim 10^5$ yr old, in good agreement with the minimum ZAMS age of the cluster and estimates of the end of the period of active gas collapse (Table 4). It is thus likely that the expanding shell is a remnant from the earlier stages of the gas-clearing phase when the outflow was stronger. It is unlikely that this shell was created by a past supernova explosion as synchrotron emission is a negligible component of this cluster's SED on 5 pc scales (E. A. C. Mills et al. 2021, in preparation).

While the SSCs in the heart of NGC 253 constitute a very young population of clusters, there is evidence for differing evolutionary stages among them. A major step toward better characterizing these clusters is better measurements of their stellar masses. Current stellar mass estimates use the 36 GHz continuum emission—assuming that it is all due to free-free emission—to calculate the ionizing photon rate and hence the stellar mass (Leroy et al. 2018). Due to the enormous extinctions toward these clusters, it is not feasible to use traditional optical and NIR recombination lines as tracers of the ionized gas. High-resolution hydrogen RRLs offer direct probes of the ionizing photon rate and hence the stellar mass, and are uninhibited by dust extinction (Emig et al. 2020 in NGC 4945, E. A. C. Mills et al. 2021, in preparation in NGC 253). In the near future, James Webb Space Telescope observations may allow us to independently establish stellar masses, radiation fields, and ages by accessing mid-IR spectral line indicators. In the next decade, the combination of sensitivity and exquisite resolution of the Next Generation VLA (ngVLA) may make studies at this high resolution possible for galaxies out to the Virgo cluster and beyond.

R.C.L. thanks Eve Ostriker for very helpful discussions and feedback that greatly improved this paper. R.C.L. also thanks Todd Thompson, Stuart Vogel, Lachlan Lancaster, and Pavel Kroupa for useful conversations and advice. The authors thank Nicolas Bolatto for his help in making the 3D visualizations for Figures 8 and B1. Publication support was provided by the NRAO. R.C.L. acknowledges support for this work provided by the NSF through the Student Observing Support Program (SOSP) award 7-011 from the NRAO. K.L.E. acknowledges financial support from the Netherlands Organization for Scientific Research through TOP grant 614.001.351. E.R. acknowledges the support of the Natural Sciences and Engineering Research Council of Canada (NSERC), funding reference number RGPIN-2017-03987. This paper makes use of the following ALMA data: ADS/JAO. ALMA#2017.1.00433.S. ALMA is a partnership of the ESO (representing its member states), NSF (USA), and NINS (Japan), together with NRC (Canada), MOST and ASIAA (Taiwan), and KASI (Republic of Korea), in cooperation with the Republic of Chile. The Joint ALMA Observatory is operated by the ESO, AUI/NRAO and NAOJ. The National Radio Astronomy Observatory is a facility of the National Science Foundation operated under cooperative agreement by Associated Universities, Inc. Based on observations made with the NASA/ESA Hubble Space Telescope, obtained from the data archive at the Space Telescope Science Institute. STScI is operated by the Association of Universities for Research in Astronomy, Inc. under NASA contract NAS 5-26555.

Facilities: ALMA, HST.

Software: Astropy (The Astropy Collaboration et al. 2018), CASA (McMullin et al. 2007), emcee (Foreman–Mackey et al. 2013), MatPlotLib (Barrett et al. 2005), NumPy (Harris et al. 2020), pandas (Reback et al. 2020), photutils (Bradley et al. 2018), SciPy (Virtanen et al. 2020), seaborn (Waskom et al. 2014).

Appendix A Measuring Outflow Properties from Fitting the Absorption Features

For each outflow candidate SSC, we measure important outflow properties based on the $\mathrm{H}^{13}\mathrm{CN}$ 4–3 and CS 7–6 spectra (Section 3.1, Table 2). Below, we explain how each of these properties is calculated. First, we fit the foreground-removed (Section 2.4) $\mathrm{H}^{13}\mathrm{CN}$ 4–3 and CS 7–6 spectra with a two-component Gaussian of the form

$$I(V) = I_{\text{max}-\text{emis}} e^{-(V-V_{\text{max}-\text{emis}})^2/2\sigma_{\text{emis}}^2}$$

$$+ I_{\text{max}-\text{abs}} e^{-(V-V_{\text{max}-\text{abs}})^2/2\sigma_{\text{abs}}^2} + I_{\text{cont}}$$
(A1)

with terms to fit the emission, absorption, and continuum components, respectively. These fits are shown in Figure 6 as the blue dashed curves. We define the outflow crossing time, which is the time it takes a gas parcel to travel from the center of the cluster to $r_{\rm SSC}$ (half the major axis FWHM sizes listed in Table 1) moving at the typical outflow velocity ($V_{\rm max-abs}$) as

$$t_{\rm cross} = \frac{r_{\rm SSC}}{V_{\rm max-abs}}.$$
 (A2)

This is a lower limit to the outflow age, assuming a constant outflow velocity, since the outflows are observed out to at least $r_{\rm SSC}$ and could be present at larger distances from the cluster. The maximum outflow velocity is defined as

$$V_{\text{out.max}} \equiv V_{\text{max-abs}} + 2\sigma_{\text{abs}}.$$
 (A3)

We determine the optical depth of the center of the absorption feature where

$$\tau_{\text{max}-\text{abs}} = -\ln\left(\frac{I_{\text{max}-\text{abs}}}{I_{\text{cont}}}\right). \tag{A4}$$

From there, we calculate the column density in the *lower* state of each molecule following Mangum & Shirley (2015)

$$N_{\ell} = 16\pi\sqrt{2\ln 2} \left(\frac{\nu_{u\ell}}{c}\right)^{2} \sigma_{abs} \frac{\tau_{max-abs}}{A_{u\ell}} [e^{h\nu_{u\ell}/kT_{ex}} + 1]^{-1}$$
 (A5)

(combining their Equations (29), (A1), and (A7)), where $\nu_{u\ell}$ is the frequency of the transition, c is the speed of light, $A_{u\ell}$ is the Einstein A coefficient for the transition, and $T_{\rm ex}$ is the excitation temperature. By replacing T_{ℓ} with $T_{\rm ex}$, we are assuming LTE, which we will assume throughout. We assume $T_{\rm ex} = 130 \pm 56$ K, which is the excitation temperatures found in these

clusters (Krieger et al. 2020). The uncertainty is the difference between this value and the excitation temperature measured at lower resolution (74 K; Meier et al. 2015). Our assumption on $T_{\rm ex}$ is a major source of uncertainty in these calculations. We then calculate the column density in the upper state

$$N_u = N_\ell \frac{g_u}{g_\ell} e^{-h\nu_{u\ell}/kT_{\rm ex}} \tag{A6}$$

(e.g., Equation (6) of Mangum & Shirley 2015, assuming the upper and lower states have the same density distribution along the line of sight). The total column density of each molecule (e.g., of all energy levels) is

$$N_{\text{mol}} = \frac{N_u}{g_u} \mathscr{Z} e^{h\nu_{u\ell}/kT_{\text{ex}}} \tag{A7}$$

(e.g., Equation (31) of Mangum & Shirley 2015), where \mathcal{Z} is the partition function calculated assuming LTE

$$\mathscr{Z} = \sum_{i} g_i e^{-E_i/kT_{\text{ex}}},\tag{A8}$$

where g_i and E_i are the degeneracy and excitation energy of each level i. We calculate \mathscr{Z} assuming LTE up to i=19 for CS and i=16 for H¹³CN.¹⁹ To convert from the column density of each molecule to the column density of H₂ in the outflow $(N_{\rm H_2}, {\rm out})$, we need to know the abundance ratio of each molecule with respect to H₂:

$$N_{\rm H_2,out} = 2 \frac{[{\rm H_2}]}{[{\rm mol}]} N_{\rm mol},$$
 (A9)

where the factor of 2 accounts for the redshifted outflowing material, assuming it is the same as the blueshifted component. The abundance ratios vary with environment, so we use those calculated in the center of NGC 253 by Martín et al. (2006), where [CS]/[H₂] = 5.0×10^{-9} and [H¹³CN]/[H₂] = 1.2×10^{-10} . The assumed abundance ratio is another large source of uncertainty in our measurements and can vary substantially by environment (e.g., van Dishoeck & Blake 1998, and references therein). We take an order-of-magnitude uncertainty on the abundance fractions, which limits subsequent calculations to order-of-magnitude precision as well (see the discussion in Section 3.1.1).

To calculate the H₂ mass along the line of sight,

$$M_{\text{H}_2,\text{out}} = 4\Sigma_{\text{H}_2,\text{out}}A = 4m_{\text{H}_2}N_{\text{H}_2,\text{out}}A,$$
 (A10)

where $m_{\rm H_2}$ is the mass of a hydrogen molecule, A is the area of the source measured from the continuum (Table 2), and the factor of 4 converts the projected area to a sphere.

From the mass in the outflow and the crossing time, we calculate the mass outflow rate ($\dot{M}_{\rm H_2,out}$), where

$$\dot{M}_{\rm H_2,out} = \frac{M_{\rm H_2,out}}{t_{\rm cross}}.$$
 (A11)

From the total gas mass of the cluster (Leroy et al. 2018) and the mass outflow rate, we calculate the gas-removal time, or the time it would take to expel all of the gas in the cluster at the

 $[\]overline{^{19}}$ Level population data are from https://www.astro.umd.edu/rareas/lma/lgm/properties/cs.pdf for CS and https://www.astro.umd.edu/rareas/lma/lgm/properties/h13cn.pdf for $H^{13}CN.$

current mass outflow rate:

$$t_{\text{remove-gas}} = \frac{M_{\text{H}_2,\text{tot}}}{\dot{M}_{\text{H}_2,\text{out}}}.$$
 (A12)

The timescale assumes that the mass outflow rate is constant with time, which is likely not the case (e.g., Kim et al. 2018). The momentum injected into the environment normalized by the stellar mass (M_*) by the outflow is

$$\frac{p_r}{M_*} = \frac{\sqrt{3} \, V_{\text{max}-abs} M_{\text{H}_2,\text{out}}}{M_*},\tag{A13}$$

assuming spherical symmetry (Leroy et al. 2018). We assume the SSC stellar masses reported by Leroy et al. (2018), and the uncertainties in these M_* measurements are discussed in Section 2.6. The kinetic energy in the outflow is

$$E_k = \frac{1}{2} M_{\rm H_2, out} V_{\rm max - abs}^2.$$
 (A14)

Values calculated using CS 7–6 and H¹³CN 4–3 for each outflow candidate are listed in Table 2 along with the propagated uncertainties.

Appendix B Outflow Modeling Details

We perform simple radiative transfer modeling of the source with varying outflow geometries and input physical parameters to constrain the outflow opening angles and orientations as described in Section 3.2.

To set up the model, we define a three-dimensional grid that is 65 (= 2^6+1) pixels in each dimension; we refer to this grid as the simulated box. The physical scale of the box is such that the length of each size is $4 \times r_{SSC}$, or twice the diameter of the SSC to be modeled. Every pixel in the box is given a fourth dimension, corresponding to the spectral axis (in terms of frequency or velocity, which we use interchangeably here). The spectral axis has $129 (= 2^7 + 1)$ channels. The velocity range of the spectral axis and hence the spectral resolution of the model is defined adaptively for each model to maximize the number of channels over the emission and absorption features. The spectral axis is centered on zero velocity (the rest frequency of the line to be modeled) and spans $\pm 4\sqrt{V_{
m max\,-abs}^2 + \Delta V_{
m out,FWHM}^2}$, where $V_{
m max\,-abs}$ and $\Delta V_{
m out,FWHM}$ are the outflow velocity and FWHM outflow velocity dispersion input into the model. This is done to optimize the velocity resolution over the velocities relevant for the cluster and outflow as opposed to picking a fixed velocity range. This is shown most clearly in Figure 7, where the portions of the spectra within the vertical line segments show the velocities actually modeled and the thin lines are extrapolations.

Once the four-dimensional box is defined, the three physical components representing the cluster and outflow are constructed. It is helpful to define coordinates related to the simulated box in Cartesian coordinates, whereas coordinates pertaining to the cluster and outflow are in spherical coordinates, as shown in Figure B1. As described in Section 3.2, the three components of the system are:

1. Dust continuum component: Shown in green in Figures 7, 8, B1, and B2 this component is a sphere with $r = r_{\rm SSC}$ and a constant (in space and velocity) temperature ($T_{\rm cont}$). The optical depth is a maximum ($\tau_{\rm cont,max}$) at the center,

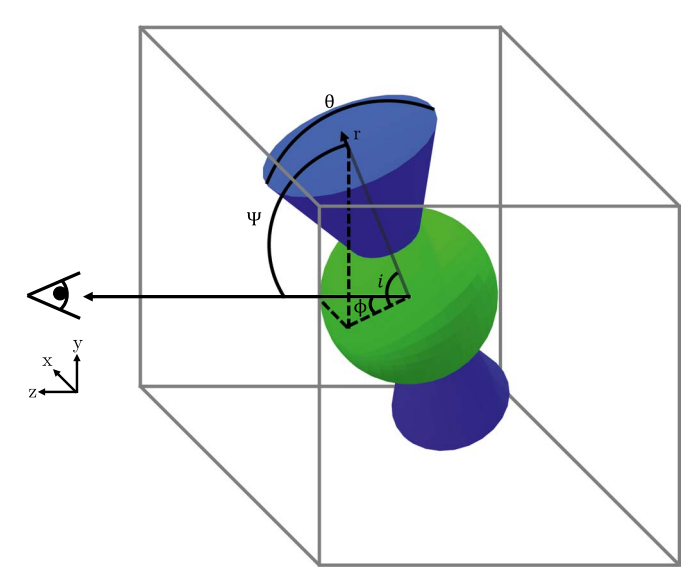


Figure B1. An example outflow, in the style of Figure 8; for clarity, the ambient gas is not shown. The simulated box is shown in gray. The orientation angle definitions are marked, where θ is the outflow opening angle and Ψ is the orientation angle to the line of sight measured from the center of the outflow cone with components i and ϕ to the x- and y-axis, respectively.

then decreases like a Gaussian with FWHM = $2 \times r_{SSC}$, so that the continuum source is semitransparent. The temperature and optical depth are set to zero for $r > r_{SSC}$.

- 2. Hot gas: Shown in yellow in Figures 7 and B2 (and encompassed within the green sphere in Figures 8 and B1), this spherical component is required to reproduce the strong emission component of the P-Cygni profiles. This component has a hot gas temperature ($T_{\rm hot}$), a central H₂ volume density ($n_{\rm hot}$), and a velocity dispersion ($\Delta V_{\rm hot,FWHM}$). $T_{\rm hot}$ is constant (spatially) for $r \leq r_{\rm SSC}$, and is set to zero outside. The density falls off $\propto r^{-2}$ from the center, and is set to zero for $r > r_{\rm SSC}$. The line is centered on zero velocity along the spectral axis, and the Gaussian line width is given by $\Delta V_{\rm hot,FWHM}/2.355$.
- 3. Cold, outflowing gas: Shown in dark blue in Figures 7, 8, B1, and B2, this is the outflow component which produces the absorption features. This component is defined by a gas temperature (T_{out}) , a maximum H_2 volume density (n_{out}) , a constant outflow velocity (V_{out}) , a velocity dispersion ($\Delta V_{\text{out,FWHM}}$), and opening angle (θ), and an orientation to the line of sight (Ψ) . The gas temperature is constant (spatially) within this component and is set to zero for $r < r_{\rm SSC}$. The density is a maximum at $r = r_{\rm SSC}$ and deceases $\propto r^{-2}$ until the edges of the box; the density is set to zero for $r < r_{SSC}$. The line is centered on along the frequency axis at $V_{\rm outflow}$, and the Gaussian line width is given by $\Delta V_{\text{out,FWHM}}$. Since the outflow velocity is constant and the density $\propto r^{-2}$, the outflow conserves energy and momentum. The outflow cones are masked to the given opening angle (θ) and rotated to the given orientation from the line of sight (Ψ) (Figure B1). For outflows with $\theta < 180^{\circ}$, the outflowing gas component outside the outflow cones is replaced by an ambient gas component (shown in light blue in Figures 8 and B2), which has the same properties as the outflowing gas but with $V_{\text{out}} = 0$. We refer to these together simply as the "cold" component.

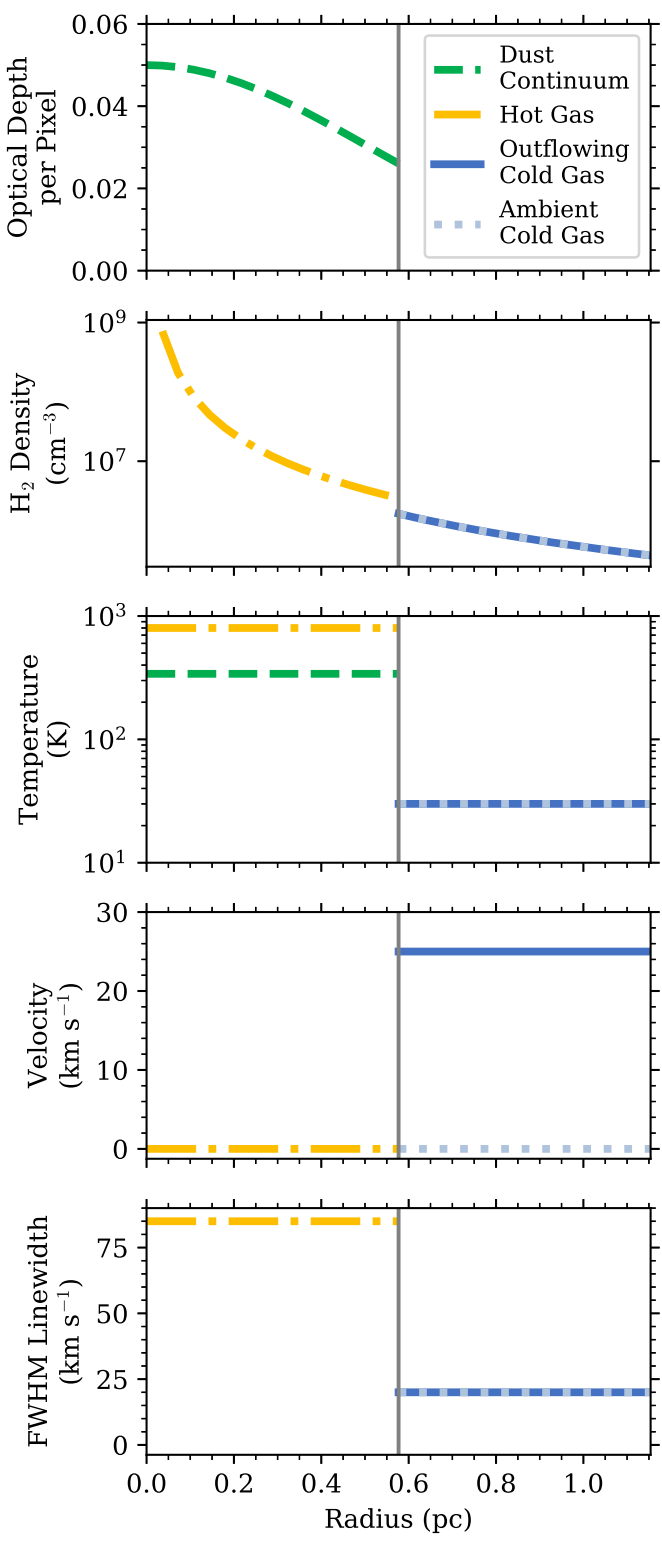


Figure B2. Radial profiles of the input parameters to the modeling for the dust continuum (green dashed), hot gas (gold dashed–dotted), outflowing cold gas (blue solid), and the ambient cold gas (light blue dotted) as described in Section 3.2. For the dust continuum, the optical depth per pixel is specified, whereas for the other components, the $\rm H_2$ density per pixel is specified. For the ambient cold gas, input parameters are identical to the outflowing cold gas except for the velocity. Cold gas inside the outflow cones has the properties of the outflowing cold gas, whereas cold gas outside the outflow cones has the properties of the ambient cold gas. The vertical gray line marks $r_{\rm SSC}$, which is the boundary between the cluster (e.g., continuum and hot gas components) and the cold gas components (outflowing or ambient). These input parameters are scaled to the best-fit spherical model for the CS 7–6 line in SSC 14 (Table 3).

The optical depths of the hot and cold (outflowing and ambient) gas are needed at every pixel and as a function of frequency ($\tau_{\nu,hot}$ and $\tau_{\nu,outflow}$, respectively) for the radiative transfer. For simplicity in the following equations, we will drop the "hot" and "cold" subscripts since the calculations are the same for both components. First, we calculate the intrinsic line shape assuming Doppler broadening is dominant

$$\phi_{\nu} = \frac{1}{\sqrt{\pi}\nu_{\nu\ell}} \frac{c}{b} e^{-V^2/b^2},\tag{B1}$$

where $b \equiv \sqrt{2}\,\sigma_V = \frac{\Delta V_{\rm FWHM}}{2\sqrt{\ln 2}}$, $\nu_{u\ell}$ is the rest frequency of the transition being modeled, and V is the velocity along the spectral axis (with $V\!=\!0$ corresponding to $\nu\!=\!\nu_{u\ell}$) and where $\int\!\!\phi_{\nu} d\nu = 1$ (Draine 2011). The absorption cross section is

$$\sigma_{\ell u}(\nu) = \frac{g_u}{g_\ell} \frac{c^2}{8\pi \nu_{u\ell}^2} A_{u\ell} \phi_{\nu}, \tag{B2}$$

where g_u and g_ℓ are the upper and lower level degeneracies and $A_{u\ell}$ is the Einstein A value of the transition (see footnote 19) (Draine 2011). Given the H_2 number density at every pixel $(n_{H_2}(x, y, z))$, the number density in the lower state of the modeled transition is

$$n_{\ell}(x, y, z) = \frac{[\text{mol}]}{[\text{H}_2]} \frac{g_{\ell}}{\mathscr{Z}} e^{-T_{\ell}/T} n_{H_2}(x, y, z),$$
 (B3)

where $\frac{[\text{mol}]}{[\text{H}_2]}$ is the fractional abundance of the molecule being modeled with respect to H_2 , $\mathscr Z$ is the partition function (Equation (A8)), $T_\ell \equiv E_\ell/k$ is the excitation energy of the lower energy state, and T is the input temperature of the gas. The absorption coefficient is then

$$\kappa_{\nu}(x, y, z) = n_{\ell}(x, y, z)\sigma_{\ell\nu}(\nu)(1 - e^{-k\nu/kT})$$
 (B4)

(Draine 2011). Finally, the optical depth of each pixel and as a function of frequency is

$$\Delta \tau_{\nu}(x, y, z) = \kappa_{\nu}(x, y, z) \Delta z, \tag{B5}$$

where Δz is the size of each pixel in the z direction (though in this simulation the pixels are equal size in all spatial dimensions).

For each component—now also including the continuum component—the intensity (expressed in Rayleigh–Jeans brightness temperature units) at every pixel and as a function of frequency is

$$\Delta T_{\nu}(x, y, z) = T[1 - e^{-\Delta \tau_{\nu}(x, y, z)}].$$
 (B6)

We perform the radiative transfer along the line of sight from the back of the box to the front (e.g., along the +z-axis):

$$T_{\nu}(x, y, z_{i}) = T_{\nu}(x, y, z_{i+1})e^{-\sum_{\text{comp}} \Delta \tau_{\nu}(x, y, z_{i})} + \sum_{\text{comp}} \Delta T_{\nu}(x, y, z_{i}),$$
(B7)

where z_i denotes an individual step along the z-axis and \sum_{comp} means a sum over the dust continuum, hot gas, and cold (outflowing and ambient) gas components.

The observed spectra are averaged over the FWHM continuum source size. To best compare with the observed spectra, we mask the simulated box of $T_{\nu}(x, y, z)$ to a cylinder along the z-axis with $r = r_{\rm SSC}$ as shown in Figure 8, setting

pixels outside this region equal to zero. The final modeled spectrum is

$$T_{\nu} = \frac{1}{N_{\text{pix}}} \sum_{x,y} T_{\nu}(x, y, z = z_{\text{max}}),$$
 (B8)

where $z = z_{\text{max}}$ denotes the slice (in the *xy*-plane) at the front of the box and N_{pix} is the number of non-masked pixels in that slice. The best-fitting modeled spectra are shown in red in Figure 6.

There are degeneracies between input parameters. The observed continuum level is a combination of the intrinsic continuum temperature (T_{cont}) and the continuum optical depth $(\tau_{\rm cont})$; a higher $\tau_{\rm cont}$ with a lower $T_{\rm cont}$ can produce the same fit as a lower $au_{\rm cont}$ with a higher $T_{\rm cont}$. The temperature and density of the hot gas component ($T_{\rm hot}$ and $n_{\rm hot}$) are linked in a similar way. Moreover, a lower $\tau_{\rm cont}$ means less of the hot gas and redshifted outflow are attenuated, and so lower T_{hot} and $n_{\rm hot}$ values are required. These degeneracies, especially with regards to the density, lead to a very uncertain total mass for the modeled cluster. The outflow parameters, however, are more robust. The gas temperature in the outflow (T_{out}) is linked to the density in the outflow (n_{out}) , but are not as degenerate as for the hot gas component for the following reason. For absorption, the minimum modeled brightness temperature cannot be less than the given T_{out} , even for an arbitrarily high density. That is, in order to match the models with the observations, the observed temperature at maximum absorption sets the maximum possible T_{out} in the model. For these reasons, though we report all input parameters for the best-fitting models, we only report derived parameters for the outflow in Table 3.

ORCID iDs

Rebecca C. Levy https://orcid.org/0000-0003-2508-2586 Alberto D. Bolatto https://orcid.org/0000-0002-5480-5686 Adam K. Leroy https://orcid.org/0000-0002-2545-1700 Kimberly L. Emig https://orcid.org/0000-0001-6527-6954 Mark Gorski https://orcid.org/0000-0001-9300-354X Nico Krieger https://orcid.org/0000-0003-1104-2014 Laura Lenkić https://orcid.org/0000-0003-4023-8657 David S. Meier https://orcid.org/0000-0001-9436-9471 Elisabeth A. C. Mills https://orcid.org/0000-0001-8782-1992 Jürgen Ott https://orcid.org/0000-0001-8224-1956 Erik Rosolowsky https://orcid.org/0000-0002-5204-2259 Elizabeth Tarantino https://orcid.org/0000-0003-1356-1096 Sylvain Veilleux https://orcid.org/0000-0002-3158-6820 Fabian Walter https://orcid.org/0000-0003-4793-7880 Axel Weiß https://orcid.org/0000-0003-4678-3939 Martin A. Zwaan https://orcid.org/0000-0003-0101-1804

References

```
Aalto, S., Muller, S., König, S., et al. 2019, A&A, 627, A147
Agertz, O., Kravtsov, A. V., Leitner, S. N., & Gnedin, N. Y. 2013, ApJ, 770, 25
Anantharamaiah, K. R., & Goss, W. M. 1996, ApJL, 466, L13
Ando, R., Nakanishi, K., Kohno, K., et al. 2017, ApJ, 849, 81
Barnes, A. T., Longmore, S. N., Dale, J. E., et al. 2020, MNRAS, 498, 4906
Barrett, P., Hunter, J., Miller, J. T., Hsu, J.-C., & Greenfield, P. 2005, in ASP Conf. Ser. 347, Astronomical Data Analysis Software and Systems XIV, ed. P. Shopbell, M. Britton, & R. Ebert (San Francisco, CA: ASP), 91
Bendo, G. J., Beswick, R. J., D'Cruze, M. J., et al. 2015, MNRAS, 450, L80
Bradley, L., Sipőcz, B., Robitaille, T., et al. 2018, Astropy/Photutils: v0.5, Zenodo, doi:10.5281/zenodo.1340699
Calura, F., Few, C. G., Romano, D., & D'Ercole, A. 2015, ApJL, 814, L14
```

```
Chabrier, G. 2003, PASP, 115, 763
Charnley, S. B. 1997, ApJ, 481, 396
Cohen, D. P., Turner, J. L., Consiglio, S. M., Martin, E. C., & Beck, S. C.
   2018, ApJ, 860, 47
Colzi, L., Fontani, F., Caselli, P., et al. 2018, A&A, 609, A129
Consiglio, S. M., Turner, J. L., Beck, S., & Meier, D. S. 2016, ApJL, 833, L6
Cordoni, G., Milone, A. P., Mastrobuono-Battisti, A., et al. 2020, in IAU
   Symp. 351, Star Clusters: From the Milky Way to the Early Universe, ed.
   A. Bragaglia et al. (Cambridge: Cambridge Univ. Press), 281
Crocker, R. M., Krumholz, M. R., Thompson, T. A., Baumgardt, H., &
   Mackey, D. 2018a, MNRAS, 481, 4895
Crocker, R. M., Krumholz, M. R., Thompson, T. A., & Clutterbuck, J. 2018b,
      NRAS, 478, 81
Davidge, T. J. 2016, ApJ, 818, 142
Davis, T. A., Bayet, E., Crocker, A., Topal, S., & Bureau, M. 2013, MNRAS,
de Pree, C. G., Gaume, R. A., Goss, W. M., & Claussen, M. J. 1996, ApJ,
Dinnbier, F., & Walch, S. 2020, MNRAS, 499, 748
Draine, B. T. 2011, Physics of the Interstellar and Intergalactic Medium
   (Princeton, NJ: Princeton University Press)
El-Badry, K., Ostriker, E. C., Kim, C.-G., Quataert, E., & Weisz, D. R. 2019,
   MNRAS, 490, 1961
Emig, K. L., Bolatto, A. D., Leroy, A. K., et al. 2020, ApJ, 903, 50
Fall, S. M., Krumholz, M. R., & Matzner, C. D. 2010, ApJL, 710, L142
Foreman-Mackey, D., Hogg, D. W., Lang, D., & Goodman, J. 2013, PASP,
   125, 306
Geen, S., Bieri, R., Rosdahl, J., & de Koter, A. 2021, MNRAS, 501, 1352
Geen, S., Hennebelle, P., Tremblin, P., & Rosdahl, J. 2015, MNRAS,
Geen, S., Pellegrini, E., Bieri, R., & Klessen, R. 2020, MNRAS, 492, 915
Gilbert, A. M., & Graham, J. R. 2007, ApJ, 668, 168
Ginsburg, A., & Kruijssen, J. M. D. 2018, ApJL, 864, L17
Gorski, M., Ott, J., Rand, R., et al. 2017, ApJ, 842, 124
Gorski, M. D., Ott, J., Rand, R., et al. 2019, MNRAS, 483, 5434
Gray, W. J., Oey, M. S., Silich, S., & Scannapieco, E. 2019, ApJ, 887, 161
Grudić, M. Y., Hopkins, P. F., Faucher-Giguère, C.-A., et al. 2018, MNRAS,
Guszejnov, D., Grudić, M. Y., Hopkins, P. F., Offner, S. S. R., &
   Faucher-Giguère, C.-A. 2021, MNRAS, 502, 3646
Harris, C. R., Millman, K. J., van der Walt, S. J., et al. 2020, Natur, 585, 357
He, C.-C., Ricotti, M., & Geen, S. 2019, MNRAS, 489, 1880
Henkel, C., Asiri, H., Ao, Y., et al. 2014, A&A, 565, A3
Herrera, C. N., & Boulanger, F. 2017, A&A, 600, A139
Johnson, K. E., Leroy, A. K., Indebetouw, R., et al. 2015, ApJ, 806, 35
Johnson, L. C., Seth, A. C., Dalcanton, J. J., et al. 2016, ApJ, 827, 33
Kamann, S., Bastian, N. J., Gieles, M., Balbinot, E., & Hénault-Brunet, V.
   2019, MNRAS, 483, 219
Keto, E., Ho, L. C., & Lo, K. Y. 2005, ApJ, 635, 1062
Kim, C.-G., & Ostriker, E. C. 2015, ApJ, 802, 99
Kim, C.-G., Ostriker, E. C., & Raileanu, R. 2017a, ApJ, 834, 25
Kim, J.-G., Kim, W.-T., & Ostriker, E. C. 2016, ApJ, 819, 137
Kim, J.-G., Kim, W.-T., & Ostriker, E. C. 2018, ApJ, 859, 68
Kim, J.-G., Kim, W.-T., & Ostriker, E. C. 2019, ApJ, 883, 102
Kim, J.-G., Kim, W.-T., Ostriker, E. C., & Skinner, M. A. 2017b, ApJ, 851, 93
Koribalski, B. S., Staveley-Smith, L., Kilborn, V. A., et al. 2004, AJ, 128, 16
Kornei, K. A., & McCrady, N. 2009, ApJ, 697, 1180
Krieger, N., Bolatto, A. D., Leroy, A. K., et al. 2020, ApJ, 897, 176
Krieger, N., Bolatto, A. D., Walter, F., et al. 2019, ApJ, 881, 43
Kroupa, P. 2001, MNRAS, 322, 231
Kruijssen, J. M. D. 2012, MNRAS, 426, 3008
Krumholz, M. R., McKee, C. F., & Bland-Hawthorn, J. 2019, ARA&A,
Lancaster, L., Ostriker, E. C., Kim, J.-G., & Kim, C.-G. 2021a, ApJ, in press
Lancaster, L., Ostriker, E. C., Kim, J.-G., & Kim, C.-G. 2021b, ApJ, in press
Lang, C. C., Goss, W. M., & Wood, O. S. 1997, ApJ, 474, 275
Leitherer, C., Schaerer, D., Goldader, J. D., et al. 1999, ApJS, 123, 3
Leroy, A. K., Bolatto, A. D., Ostriker, E. C., et al. 2015, ApJ, 801, 25
Leroy, A. K., Bolatto, A. D., Ostriker, E. C., et al. 2018, ApJ, 869, 126
Lochhaas, C., & Thompson, T. A. 2017, MNRAS, 470, 977
Löckmann, U., Baumgardt, H., & Kroupa, P. 2010, MNRAS, 402, 519
Lu, J. R., Do, T., Ghez, A. M., et al. 2013, ApJ, 764, 155
Maccarone, T. J., Lehmer, B. D., Leyder, J. C., et al. 2014, MNRAS, 439,
Mangum, J. G., & Shirley, Y. L. 2015, PASP, 127, 266
Mapelli, M. 2017, MNRAS, 467, 3255
```

```
Marks, M., Kroupa, P., Dabringhausen, J., & Pawlowski, M. S. 2012,
   MNRAS, 422, 2246
Martín, S., Aladro, R., Martín-Pintado, J., & Mauersberger, R. 2010, A&A,
  522, A62
Martín, S., Mauersberger, R., Martín-Pintado, J., Henkel, C., &
   García-Burillo, S. 2006, ApJS, 164, 450
Martín, S., Muller, S., Henkel, C., et al. 2019, A&A, 624, A125
McMullin, J. P., Waters, B., Schiebel, D., Young, W., & Golap, K. 2007, in
   ASP Conf. Ser. 376, Astronomical Data Analysis Software and Systems
   XVI, ed. R. A. Shaw, F. Hill, & D. J. Bell (San Francisco, CA: ASP), 127
Meier, D. S., Walter, F., Bolatto, A. D., et al. 2015, ApJ, 801, 63
Mezger, P. G., & Smith, L. F. 1976, A&A, 47, 143
Murphy, E. J., Condon, J. J., Schinnerer, E., et al. 2011, ApJ, 737, 67
Murray, N., Quataert, E., & Thompson, T. A. 2010, ApJ, 709, 191
Nayak, O., Meixner, M., Sewiło, M., et al. 2019, ApJ, 877, 135
Oey, M. S., Herrera, C. N., Silich, S., et al. 2017, ApJL, 849, L1
Olivier, G. M., Lopez, L. A., Rosen, A. L., et al. 2021, ApJ, 908, 68
Ossenkopf, V., & Henning, T. 1994, A&A, 291, 943
Paglione, T. A. D., Yam, O., Tosaki, T., & Jackson, J. M. 2004, ApJ, 611, 835
Palouš, J., Wünsch, R., & Tenorio-Tagle, G. 2014, ApJ, 792, 105
Portegies Zwart, S. F., McMillan, S. L. W., & Gieles, M. 2010, ARA&A,
Rahner, D., Pellegrini, E. W., Glover, S. C. O., & Klessen, R. S. 2017,
Rahner, D., Pellegrini, E. W., Glover, S. C. O., & Klessen, R. S. 2019,
   MNRAS, 483, 2547
Raskutti, S., Ostriker, E. C., & Skinner, M. A. 2017, ApJ, 850, 112
Reback, J., McKinney, W., Brockmendel, J., et al. 2020, in pandas-dev/
   pandas: Pandas v1.1.3, Zenodo doi:10.5281/zenodo.4067057
Rekola, R., Richer, M. G., McCall, M. L., et al. 2005, MNRAS, 361, 330
Rico-Villas, F., Martín-Pintado, J., González-Alfonso, E., Martín, S., &
   Rivilla, V. M. 2020, MNRAS, 491, 4573
```

```
Sakamoto, K., Ho, P. T. P., Iono, D., et al. 2006, ApJ, 636, 685
Sakamoto, K., Mao, R.-Q., Matsushita, S., et al. 2011, ApJ, 735, 19
Schneider, F. R. N., Sana, H., Evans, C. J., et al. 2018, Sci, 359, 69
Schöier, F. L., van der Tak, F. F. S., van Dishoeck, E. F., & Black, J. H. 2005,
  A&A, 432, 369
Semenov, D., Henning, T., Helling, C., Ilgner, M., & Sedlmayr, E. 2003, A&A,
  410, 611
Shirley, Y. L. 2015, PASP, 127, 299
Silich, S., Tenorio-Tagle, G., & Rodríguez-González, A. 2004, ApJ, 610, 226
Skinner, M. A., & Ostriker, E. C. 2015, ApJ, 809, 187
Sokal, K. R., Johnson, K. E., Indebetouw, R., & Massey, P. 2016, ApJ,
  826, 194
Tang, X. D., Henkel, C., Menten, K. M., et al. 2019, A&A, 629, A6
The Astropy Collaboration, Price-Whelan, A. M., Sipőcz, B. M., et al. 2018,
  AJ, 156, 123
Thompson, T. A., & Krumholz, M. R. 2016, MNRAS, 455, 334
Turner, J. L., Beck, S. C., Benford, D. J., et al. 2015, Natur, 519, 331
Turner, J. L., Consiglio, S. M., Beck, S. C., et al. 2017, ApJ, 846, 73
Turner, J. L., & Ho, P. T. P. 1985, ApJL, 299, L77
Ulvestad, J. S., & Antonucci, R. R. J. 1997, ApJ, 488, 621
van Dishoeck, E. F., & Blake, G. A. 1998, ARA&A, 36, 317
Vink, J. S., & de Koter, A. 2005, A&A, 442, 587
Virtanen, P., Gommers, R., Oliphant, T. E., et al. 2020, Nature Methods,
  17, 261
Waskom, M., Botvinnik, O., Hobson, P., et al. 2014, Seaborn v0.5.0, Zenodo,
  doi:10.5281/zenodo.12710
Watson, A. M., Gallagher, J. S. I., Holtzman, J. A., et al. 1996, AJ, 112, 534
Weaver, R., McCray, R., Castor, J., Shapiro, P., & Moore, R. 1977, ApJ,
Wünsch, R., Palouš, J., Tenorio-Tagle, G., & Ehlerová, S. 2017, ApJ, 835, 60
Zapartas, E., de Mink, S. E., Izzard, R. G., et al. 2017, A&A, 601, A29
Ziurys, L. M., & Turner, B. E. 1986, ApJL, 300, L19
```